Accepted Manuscript

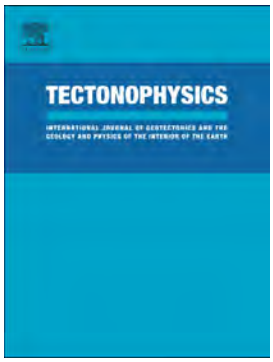

Structural characteristics, bulk porosity and evolution of an exhumed long-lived hydrothermal system

Daniel Egli, Rahel Baumann, Sulamith Küng, Alfons Berger, Ludovic Baron, Marco Herwegh

PII: S0040-1951(18)30328-7
DOI: doi:10.1016/j.tecto.2018.10.008
Reference: TECTO 127947

To appear in: *Tectonophysics*

Received date: 12 December 2017
Revised date: 30 September 2018
Accepted date: 5 October 2018

Please cite this article as: Daniel Egli, Rahel Baumann, Sulamith Küng, Alfons Berger, Ludovic Baron, Marco Herwegh , Structural characteristics, bulk porosity and evolution of an exhumed long-lived hydrothermal system. Tecto (2018), doi:10.1016/j.tecto.2018.10.008

Structural characteristics, bulk porosity and evolution of an exhumed long-lived hydrothermal system

Daniel Egli[1], Rahel Baumann[1], Sulamith Küng[1], Alfons Berger[1], Ludovic Baron[2], Marco Herwegh[1]

[1]Institute of Geological Sciences, University of Bern, Baltzerstrasse 1+3, 3012 Bern, Switzerland

[2]Institute of Earth Sciences, University of Lausanne, Bâtiment Geopolis, 1015 Lausanne, Switzerland

Corresponding author:

Daniel Egli (daniel.egli@geo.unibe.ch)

Abstract

The geometry and spatial variability of fracture networks and matrix porosity of fault rocks are key parameters controlling the permeability and ultimately the fluid flux along fault zones. Detailed understanding of evolution and long-term sustainability of naturally porous and permeable fault rocks is thus of prime importance for predicting the occurrence and the successful exploration of natural fault-bound hydrothermal systems. This study presents continuous structural data and matrix porosity measurements collected from a cored drillhole across a long-lived and still active fault-bound hydrothermal system in the crystalline basement of the Aar Massif (Swiss Alps). Image analysis and He-pycnometry analysis for quantification of matrix porosity of tectonites showing variable ductile and brittle deformation intensity is combined with fracture porosity calculations to develop a bulk porosity profile across this hydrothermally active fault zone. In the investigated example, a central fault core that shows a several meter wide fault breccia with consolidated gouge material of increased porosity with maximum values of 9% (He-pycnometry) and >20% (image analysis) is adjoined by several large subsidiary faults and interconnected by a intensly fractured damage zone embedded in granitic to ultramylonitic host rock showing 0.1-6% porosity. The variable degree of ductile precursors forms a succession of subparallel sealing and high-porosity structures parallel to the fault zone bridged by a dense fracture network. Fluid flow is therefore directly related to the combined

effect of fractures and enhanced fault-related matrix porosity, possibly dynamically changing with time due to fracturing and precipitation cycles. This suggests a key importance of matrix porosity within fault core rocks (breccia & fault gouge) for the transport of hydrothermal fluids.

Keywords:

- Multi-scale porosity
- Hydrothermal circulation
- Orogenic hydrothermal systems

1 Introduction

The spatial distribution, orientation and continuity of brittle and ductile structures in the Earth's crust strongly control fluid pathways in a rock mass by joining existing pores and creating new pore space (fractures, joints) but can also act as seals to fluid flow (e.g. ductile shear zones, clay-rich fault gouges) [e.g. *Sibson*, 1986; *Caine et al.*, 1996; *Evans et al.*, 1997]. Understanding the detailed fluid flow paths in tight reservoir rocks is therefore crucial for applied geological problems such as radioactive waste disposal, CO_2 sequestration or geothermal energy production. Naturally porous and permeable rock masses could, for example, serve as an alternative to enhanced geothermal systems (EGS), which have in the past produced inacceptable levels of induced seismicity and/or insufficient production rates (e.g. induced earthquakes with a maximum magnitude of 3.4 in the exploration well of Basel, Switzerland, in 2006; [*Häring et al.*, 2008]). Successful exploration of hydrothermal systems for energy production, apart from the required heat, largely relies on sufficient permeability that can be accessed for fluid circulation, which itself is a function of the rock's properties (e.g. matrix porosity) and its structural framework (e.g. fracture porosity or sealing structures).

Orogenic hydrothermal systems are an often-observed feature and many examples of such systems are known in the European Alps and several have been proven to have a water circulation down to depths of >5 km (e.g. Grimsel Pass, Lavey-les-Bains, Saint-Gervais-les-Bains [e.g. *Bianchetti et al.*, 1992; *Hofmann et al.*, 2004; *Sonney and Vuataz*, 2009]. However, in long-lived hydrothermal systems, permeability and the related fluid flow paths are dynamic in space and time. Fault zones often have complex structures that depend on a multitude of parameters such as lithology, tectonic environment, depth, displacement and presence of fluids [e.g. *Wibberley et al.*, 2008; *Mitchell and Faulkner*, 2009; *Faulkner et al.*, 2010]. They generally consist of one or several fault cores containing cataclastic and fault gouge material. The latter are surrounded by a damage zone of increased fracture and fault density, which decreases in intensity with distance from the fault core, marking the transition to the unaffected country rock altering the porosity and permeability of the affected rock mass dramatically [*Faulkner et al.*, 2010]. Understanding the evolution, behaviour and 3D geometries (lateral extension, dimension, depth range) of naturally porous and permeable rock masses is critical for the successful exploration and sustainable exploitation of hydrothermal systems and can advance methods for

planning and implementation of enhanced geothermal systems. In low-enthalpy geological settings where no extreme geothermal gradient and heat flow (as e.g. in volcanic regions) can be observed, as is the case in wide parts of continental Europe, depths of at least 4-5 km have to be reached for efficient electricity production assuming an average geothermal gradient of 25-30°C [e.g. *Fridleifsson et al.*, 2008].

Due to the common inaccessibility of active hydrothermal reservoirs of suitable depth, e.g. in the northern Alpine foreland of the European Alps, where target rock units are buried beneath several km thick sedimentary sequences, direct observations on potential reservoir rocks are often impossible and the knowledge about the size, fluid pathways and porosity/permeability of such systems is still insufficient. As an analogue study for deep hydrothermal systems, this study focuses on an active fault-bound hydrothermal system in the crystalline basement of the Aar Massif (hydrothermal field Grimsel Pass, Swiss Alps) that has been exhumed from few kilometres depth and which documents at least 3 Ma of hydrothermal activity [*Stalder*, 1964; *Hofmann et al.*, 2004; *Belgrano et al.*, 2016]. More generally, it represents an analogue for potential geothermal reservoirs in the deep (4-5 km) crystalline subsurface of the northern Alpine foreland as well as for other hydrothermal springs in and around the Aar and Aiguilles Rouges massifs (e.g. Brigerbad, Leukerbad, Lavey-les-Bains) and, in a broader context, for orogenic hydrothermal systems worldwide.

Detailed structural data collected from a 125.3 m long drillhole across the hydrothermal zone, the corresponding drill core and surface mapping are combined for the characterization of natural hydrothermal systems with regard to its structural evolution and, more specifically, porosity, fracture distribution and fluid-flow reconstruction. The study area shows a multitude of similarly striking fault zones of comparable appearance [e.g. *Baumberger*, 2015; *Wehrens et al.*, 2017], with only one showing signs of hydrothermal activity. The lack of obvious distinguishing features between hydrothermally active and inactive fault zones in the study area shows the need for detailed understanding of the evolution, preservation and isolation of such zones. To that end, the relationships between ductile precursor structures developed during Alpine orogeny and brittle overprint during the exhumation of the Aar Massif in the surrounding of the Grimsel hydrothermal zone are analyzed to establish the fault architecture. Porosity across the structure related to that fracture pattern (i.e.

fracture porosity) as well as matrix porosity within the meta-granite that has been heterogeneously ductilely and brittely deformed to variable degree is quantified and interpreted with respect to its evolution and potential for fluid conductivity.

2 Geological setting

The study area is located in the central Aar Massif on the Grimsel Pass in central Switzerland (Fig. 1). The explored rock units of the Aar Massif form part of the External Crystalline Massifs (ECM), which represent exhumed basement rocks of the former Mesozoic European continental margin consisting of pre-Variscan polymetamorphic basement, Late- to post-Variscan intrusives and Palaeozoic sediments [e.g. *Abrecht*, 1994]. The Central Aar Massif is composed mainly of pre-Variscan basement intruded by the Late Carboniferous Haslital granitoid intrusive suite comprising, the Grimsel granodiorite, the Central Aar granite and the Southwestern Aar granite [*Schaltegger*, 1990; *Schaltegger and Corfu*, 1992; *Berger et al.*, 2016]. The Ausserberg-Avat zone and the Grimsel zone mainly represent polymetamorphic gneisses in which the Post-Variscan plutonite suite (SW-Aar granite, Grimsel granodiorite and Aplitic boundary facies) intruded (Fig. 1).

Approximate position of figure 1

For more detailed information on the corresponding lithologies, the reader is referred to Stalder [1964] and Berger et al. [2016]. While the pre-Variscan polymetamorphic basement underwent a long and complex deformation history, the post-Variscan intrusions were merely affected by the Alpine orogeny and thus recorded mainly an Early Miocene to present deformation history [*Rolland et al.*, 2009; *Wehrens et al.*, 2017]. The central Aar Massif is characterized by a dense shear zone network that shows a predominant alignment of ENE-WSW striking major shear zones cross-cut by NW-SE and NE-SW striking interconnecting shear zone systems [*Steck*, 1968; *Choukroune and Gapais*, 1983; *Pfiffner et al.*, 1997; *Rolland et al.*, 2009; *Baumberger*, 2015; *Wehrens et al.*, 2017]. These shear zones preferentially show a NE-SW trend, are mostly steeply SE dipping and show SE trending down dip lineation with preferential reverse as well as subordinate normal faulting senses of shear [*Wehrens*

et al., 2017]. These shear zones originated under mainly ductile deformation at peak metamorphic conditions (T ~450°C, 6kbar [*Goncalves et al.*, 2012; *Wehrens et al.*, 2016; *Wehrens et al.*, 2017]; 22 – 17 Ma, [*Challandes et al.*, 2008; *Rolland et al.*, 2009]). With exhumation and retrograde cooling the Aar Massif experienced a change from vertical to horizontal tectonics, expressed by NW directed thrusting and associated exhumation of the entire Aar Massif above a crustal ramp system [*Herwegh et al.*, 2017; Herwegh et al., in review]. In the Grimsel area, pronounced strain partitioning led to the reactivation of the former reverse/normal faults as dextral oblique to strike-slip faults [*Rolland et al.*, 2009; *Wehrens et al.*, 2016; *Wehrens et al.*, 2017]. Most prominent is the crustal-scale Grimselpass shear zone (GPSZ), which consists of a ENE-WSW trending set of 3-5 major shear zones interconnected with secondary shear zone bridges, the latter being discontinuously distributed (Fig. 2a; [*Baumberger*, 2015; *Wehrens et al.*, 2016; *Wehrens et al.*, 2017]). The major shear zones have thicknesses of several meters and spacings between several tens and up to 200 meters. The onset of strike slip shearing occurred under still ductile conditions (quartz dynamically recrystallizing, biotite stable) at 14-12 Ma as inferred from white mica radiometric and zircon fission track dating [*Michalski and Soom*, 1990; *Rolland et al.*, 2009; *Berger et al.*, 2017]. With progressive strike slip shearing and cooling the rheology changed towards a brittle deformation style [*Wehrens et al.*, 2017], where the brittle-ductile transition of the GPSZ is dated by quartz fissures at about 11.5 Ma [*Bergemann et al.*, 2017]. After this time, deformation is inferred to preferentially occur under brittle conditions in the Grimsel area (e.g. fault gouges of 10.4-6.6 Ma, [*Kralik et al.*, 1992]; 13.6-8.3 Ma [*Pleuger et al.*, 2012]; cleft age of monazite growth of 7 Ma [*Bergemann et al.*, 2017]). Structurally, deformation localizes along some of the GPSZ's ENE-WSW trending segments of the former major shear zones forming brittle faults with E-W trending linkage zones in between (Fig. 2a, [*Belgrano et al.*, 2016]). This brittely active part of the GPSZ is referred to as Grimsel Breccia Fault (GBF), characterized by fault cores consisting of breccias, cataclasites and fault gouges [*Hofmann et al.*, 2004; *Belgrano et al.*, 2016] and 10-20 meters wide fractured damage zones at the transition between host rocks and fault cores on either side [*Belgrano et al.*, 2016]. The hydrothermal breccia consists of mainly angular poorly sorted clasts of host rock material ranging from several cm to <1 µm in size [*Hofmann et al.*, 2004]. With 3.3 Ma a newly grown adularia out of a breccia represents the youngest radiometric age

[*Hofmann et al.*, 2004]. Note that neither for the GPSZ nor the GBF estimates on fault displacements and fault-accommodated strain exist owing to the lack of strain markers. At present there is no structural or seismic evidence for recent activity on the GBF itself, but there is an overall background seismicity in the Grimsel area [*Belgrano et al.*, 2016].

Starting from the early evolution of the ductile shear zones around 20-22 Ma to the present day the link between deformation and fluid always played a major role. While the local formation of quartz veins and hydration of early shear zones were associated with episodic brittle deformation events [*Wehrens et al.*, 2016], a major fluid pulse is suggested for the transition between reverse/normal faulting and strike-slip faulting at 14-12 Ma [*Challandes et al.*, 2008; *Wehrens et al.*, 2016; *Bergemann et al.*, 2017; *Berger et al.*, 2017]. With the transition from ductile to brittle faulting the GPSZ in general, and the Grimsel Breccia Fault in particular, the fault rocks became accessible for pervasive fluid flux [*Belgrano et al.*, 2016]. Based on hydrothermal mineralization (different microcrystalline quartz variations, adularia, sulphides (mainly pyrite), clays, and locally fluorite; see [*Hofmann et al.*, 2004] for compositions and images), Belgrano et al. [*2016*] suggested two distinguished pipe-like upwelling zones of hydrothermal water: one in the "Sidelhorn" linkage zone and the other one at the brittle fault strand at Totensee ("Grimsel pass – Gletsch damage zone") outlning the extent of the paleohydrothermal field (Fig. 2a and b).

Approximate position of figure 2

The Grimsel hydrothermal field

Given the aforementioned structural preconditioning by large-scale fault zones and associated underground pathways for circulating water, the Aar Massif hosts numerous thermal springs on its southern border and adjacent areas in the Swiss Rhône valley and furthermore represents the exhumed equivalent the deep crystalline subsurface of the northern Alpine foreland basin. In this study, we focus entirely on the Totensee strand of the paleohydrothermal field, which is entirely situated in the metagranite of the SW Aar granite (SWAGr). It shows a relatively low background strain, which resulted in a weak foliation barely distinguishable in hand-specimen and thin section and has the

appearance of intact granite. This can be considered the low-strain end-member of ductile deformation and qualifies as host rock for all subsequent deformation.

Present-day hydrothermal activity on the Grimsel Pass has been recognised from subthermal springs in the village of Gletsch (18°C, 1758 m.a.s.l.) and in the Transitgas AG tunnel (up to 28°C) crossing the southern Aar Massif below Grimsel pass at an elevation of 1908 m.a.s.l., notably being the highest discharge of hydrothermal waters in the European Alps (Fig. 2) [*Hofmann et al.*, 2004; *Sonney and Vuataz*, 2008]. These present-day hydrothermal waters exfiltrating in the tunnel ~200 m below Grimsel pass show a mixed composition of recent meteoric waters and 40-50% of older geothermal waters that are estimated to have infiltrated some 30 ka ago and reached temperatures of at least 110-120°C corresponding to several km circulation depth [*Waber et al.*, 2017]. The surface expression of the Grimsel hydrothermal field represents a morphological incision of several km length between Gletsch and Lake Oberaar (Fig. 3a) and formed along a structure named the Grimsel Breccia Fault (GBF) [*Belgrano et al.*, 2016]. Over large parts, the GBF follows precursory ductile shear zones but also forms linkage zones between such shear zones and shows in its centre a hydrothermal breccia of few cm to several meters width (Fig. 3b) [*Stalder*, 1964; *Belgrano et al.*, 2016]. Common mineralization of SiO_2 varieties (e.g. chalcedony) in the vicinity of the hydrothermal breccia zone of the GBF (Figs. 1 & 3c) indicates flow of thermal fluids and related mineralization outside of the central breccia zone and thus suggests elevated porosity/permeability allowing infiltration of thermal waters also into the country rock.

Approximate position of figure 3

3 Approach and methodology

A combination of multiscale methods was applied to fully describe and understand the detailed geometry of the fracture network and porosity surrounding the main GBF fracture zone from the micrometre to decametre scale, with main focus on the flow path evolution with time. The applied methods included classical structural field observation, mapping and analysis of drillcore material combined with structural evaluation of drillhole optical televiewer (TV) imaging and microstructural

analysis, with main focus on porosity measurements of drillcore and surface samples. In addition, a rock-wall temperature profile, using an infrared thermometer, and structural analysis of the Transitgas AG tunnel running N-S below the Grimsel region has been performed.

The drillhole GDP-1 that has been drilled for this study is located on Grimsel Pass (46°33´39´´ N 8°20´40´´E, Fig. 2) at an elevation of 2162 m a.s.l. The inclined drillhole has a diameter of 95.76 mm (HQ standard) an azimuth of 159° and an inclination of 67°. The drillhole length of 125.3 m therefore reached a true vertical depth (TVD) of 115.1 m and a true horizontal distance (THD) of 49.5 m. The drillhole has been cored over its entire length with core diameter of 61.1 mm.

The full structural characterization of the fracture network included all measurable parameters such as orientation, aperture, spacing (orthogonal distance between two fractures with the same orientation), fracture density (number of fractures per metre along a reference line) and kinematic indicators. Fracture statistics have been calculated along a horizontal projection of the drillhole serving as reference line and distances are indicated either as distance along this reference line (true horizontal distance, THD) or in length along drillhole. In case of both structural tunnel and drillhole data, a moving average approach has been applied using different sample windows around central values along the reference line (100 m for the tunnel log and 0.5, 1 and 5 m intervals normalized to 1 m for the drillhole log). Applying such an approach with various sampling windows allows continuously resolving small-scale fluctuations as well as large-scale trends in fracture density to assess scale-dependent variations in the data, which is more informative than applying simple count of fracture density in fixed intervals.

The TV imaging provided a continuous log of the drillhole, with the exception of drilling meters 75-82 where the drillhole had to be cemented for stabilization purposes. Note it is this mechanically unstable zone, which plays a major role for fluid circulation (see below). Fractures intersecting the drillhole appear as sinusoidal lines on the 360° image of the drillhole wall. While this continuous log allowed for detailed analysis of fracture orientation, aperture, fracture density and spacing, their length and kinematic indicators had to be established from surface outcrops. Structural surface mapping on selected outcrops and transects across the GBF was then used for comparison and calibration with the dense dataset from optical TV log analysis. The kinematic information from

surface outcrops was extrapolated to the drilled section along which only few kinematic indicators could be recognized in the drillcore.

As the entire length of the drillhole is situated within the SWAGr, only structural mapping was conducted with special focus on deformation structures (ductile deformation intensity, brittle fractures and open porosity). Ductile deformation intensity was mapped continuously over the drillcore and qualitatively summed using a moving average approach for identification of spatial differences in ductile deformation. According to the ductile deformation intensity a rock classification scheme was developed.

Structural data is given in dip-direction/dip notation and shown in lower hemisphere equal-area projections (Lambert azimuthal projection). Stereoplots, the rotation of drillhole data and the calculation of mean vectors for the spacing and of the intersection lines were generated in Stereonet9.5 [*Marrett and Allmendinger*, 1990; *Allmendinger*, 2016]. Kinematic data were processed and illustrated with FaultKin7.5 [*Marrett and Allmendinger*, 1990; *Allmendinger et al.*, 2012]. Furthermore, a key outcrop (46°33′41″N, 8°20′56″E) across the central fracture zone within the deeply incised gully hosting the GBF provides the only available information on the hydrothermal breccia.

Porosity was estimated in different scales and with different methods:

1. Mesoscale (cm to meters)

Structures of <mm to several cm aperture (mainly fractures) observable in the TV log were used to estimate fracture porosity by calculating ellipses from the fracture intersection with drillhole, multiplication with the respective apertures, and calculating fracture volume percentages considering the observed drillhole section as representative elementary volume (REV). We developed this approach by ourselves and are not aware if other studies did similar steps.

2. Microscale (cm to micrometers)

Representative samples were selected to estimate the amount and types of porosity. Pore space has been analysed on photographs either of polished hand specimen or thin sections by image analysis

using ImageJ software [e.g. *Heilbronner and Keulen*, 2006; *Schneider et al.*, 2012; *Heilbronner and Barrett*, 2013; *Schindelin et al.*, 2015].

UV-images from impregnated thin sections are used for a first set of image analyses. Sample blocks have been impregnated with a resin mixed with a fluorescent agent (60:40 mixture of Araldit DY 026SP® and Laramin 260®), dried in a vacuum chamber to provide maximum saturation, and standard polished thin sections have subsequently been prepared. Microphotographs were taken from these thin sections (100x magnification) on a UV microscope (OLYMPUS BX51) equipped with a MIA-scan stage [e.g. *Frieg et al.*, 1998; *Schild et al.*, 2001].

In order to spatially resolve porosity on the scale of micrometers, representative portions of the same sections were subsequently photographed in BSE mode on a scanning electron microscope (SEM, ZEISS EV050). In order to have representative element volumes in different scales, image mosaics from the UV-microscope as well as the SEM were used.

The variability of pore sizes requires a cascade investigation. The large fractures were selected on the base of the UV-intensity at a 100x magnification. A cut off was set at fracture areas of 20 pixels (~ 8 μm^2), where smaller sizes were not considered anymore as large fractures. The left over pore sizes (<20 pixels) of each thin-section were further subdivided into different matrix-types (see table 1, section 4.4), which are identified by light microscopy and their proportions per thin section were measured by image analysis. After measuring different areas for each matrix type in different thin sections, the calculated average porosity for each matrix type that has been individually determined from high-resolution SEM images and the individual fracture porosity assessed from UV-light microscopy are combined to calculate a microscale-bulk-porosity (see Table 1). These porosity estimates are done on the area of the complete thin-section (~8 cm^2).

The image analysis approach includes the general artefacts related to sampling and sample preparation. To minimize those effects, samples have been impregnated with epoxy resin before preparation. The bulk error related to the porosity analysis results from (i) analytical error of the image analysis, (ii) potential artefacts from preparation, and (iii) extrapolation of analysed areas. The analytical error due to image quality and thresholding is small and in the range of 0.5%. Error calculations have to account the different quality of the matrix types. A small error in the definition of

matrix types will have large effect, because of the cascade approach applied in this study. This is only relevant for samples including highly mixed matrix types (= ductile sample series; top rows of Table1). This is counterbalanced by the better precision of individual matrix porosity measurements in these types (Table 1b). The breccias show higher uncertainty of matrix-type measurement, but no error is related to definition of different matrix type. Quality of matrix measurements (including potential artefacts from preparation) depends on the size of the pores (the smaller the pores the larger the relative error will be). A total error of porosity estimate by image analysis is difficult to assess, but a relative error of ~10% is a possible approximation.

The image analyses are done on sections, but all volume relations are assumed to have the same value in 2D and 3D (see [*Heilbronner and Barrett*, 2013], page 184). This would be only wrong for highly anisotropic volume distribution (see discussion).

In order to evaluate (i) the quality of the performed 2D image analysis approach, (ii) the effect of potential sample preparation artefacts as well as (iii) the effect of pore distribution in 3D, a granitic host rock (low porosity) and a fault breccia (high porosity) as two end member samples have been investigated by X-ray micro-computer-tomography (micro-CT). Small drill cores of 25 mm diameter and height have been scanned using a Bruker microCT SkyScan 2211 at University of Fribourg. Acquired data was corrected for beam hardening and ring artefacts. The images were segmented and estimated for porosity using the software Bruker CT-Analyser v.1.13). The final resolution of a voxel side was 4 µm. The uncertainty in the obtained porosity was estimated to be ~20%. This value is sufficient for evaluating the quality of the 2D imaging approach presented above.

3. He-pycnometry

Helium-pycnometry was additionally used to measure the connected and the effective porosity of the samples using a He-pycnometer (AccuPyc II 1340 V1.05) at University of Bern. In order to define the bulk volume of each sample measured from a precisely defined shape, we used drill-cores in the size between 25 and 14 mm. Diameter and length of the resulting cylinder were measured several times with an accuracy of 0.01 mm. In examples where drilling was not possible, the volumes of irregular shaped samples were measured on paraffin-coated samples and volumes were estimated by

Archimedes principle. The He-pycnometer determines the effective volume, and together with the independently weighed mass, the density of the sample is calculated. In addition, powder densities were estimated using the He-pycnometer. These input data can be used for calculating the connected or the effective porosity of the sample [*Viana et al.*, 2002; *Anovitz and Cole*, 2015]. The connected porosity is defined on the basis of the measured volume ratios:

$$\phi_{connected}\ [\%] = (1\text{-}V_{skeleton}/V_{bulk}) * 100$$

whereas the so-called "effective-porosity" is based on the density data:

$$\phi_{effective}\ [\%] = (1\text{-}\rho_{bulk}/\rho_{grain}) * 100$$

The results of the two analysis types have been treated as one dataset for this study.

4 Results

4.1 Large-scale section and drillhole

The tunnel profile below the Grimsel area runs roughly N-S (Fig. 1) crossing the GBF at a depth of 260 m below surface. Figure 4a presents the rock-wall temperature along the tunnel profile, and ductile shear zones as well as fracture density as a moving average with 100 m sampling intervals. The temperature profile shows a clear peak below the drilling location at 1500 m corresponding to the GBF at surface. Structural data were compiled from the original tunnel log [*Schneider*, 1974]. Brittle separation structures are often not distinguishable between faults with a clear offset and fracturing without offset in tunnel and drillhole logs. Consequently fractures are used as a general term for brittle separation structures. Mapped fracture orientations follow the regional trend of WSW-ENE striking subvertical fractures and they show a fracture density distribution between 5 and 30 mappable faults per 100 m interval (Fig. 4bc). A number of zones (15-18) of high fracture density occur in relatively regular intervals of 100-200 m and often correspond well with zones of high ductile deformation. However, it is important to note that only one of these zones at tunnel length 1500 m correlates with the enhanced temperature observed in the tunnel (green arrow, Fig. 4b).

Approximate position of figure 4

4.2 Drillhole overview

The drillhole as well as the important outcrops used for this study lie in their entity in the SWAGr unit of the Aar Massif. In the studied section, the SWAGr exhibits variable degrees of ductile and brittle deformation and for the subdivision for core- and surface mapping four ductile and two brittle deformation groups have been defined. Deformation intensity has been classified from weakly deformed granite (Gr if fresh, Gr-s if it shows a brownish staining) to an ultramylonite (UM) endmember of ductile deformation with two intermediate classes of moderately schistose gneiss (Gn if fresh, Gn-s if it shows a brownish staining) and mylonite (My) in between (Fig. 5). The drillhole has been classified accordingly, resulting in a continuous section of ductile deformation intensity where no core loss and cementation of the drillhole hindered data collection (Fig. 5). Brittle fault rocks have been classified into cataclasites (Ca) and fault breccia of the central fracture zone (FB). All subsequent porosity and fracture analyses were made in terms of that initial classification of tectonites.

Of the 125.3 m long drillhole, the first 2 m were in gravel, leaving 123.3 m relevant drillhole and core material. Some 12 m of the drilling length was subject to core loss (10%) occurring mainly in three zones of significant core loss between (i) 47.3-48.4, (ii) 73.1-85.9 and (iii) 96.5-96.8 m. Most of the core loss occurred above and below the targeted hydrothermal breccia zone (ii). Core loss occurred due to technical difficulties during drilling and/or in zones of highly fractured rocks and non-cohesive, medium- to coarse-grained fault gouge material.

Over the entire core section, 52% of the drillhole has been classified as weakly deformed granite, 25% as moderately schistose, 6% as mylonite, and 7% ultramylonite/shear zone. Due to the large amount of core loss in the central fracture zone, only 1.2 m (1%) was recognized in the core material as hydrothermal breccia.

Approximate position of figure 5

4.3 Ductile deformation structures

Ductile shear zones in the study area follow the regional pattern of dominantly ENE-WSW running steep shear zones [e.g. *Choukroune and Gapais*, 1983; *Wehrens et al.*, 2017]. A total of 110 foliation and 49 shear zone measurements were taken from the drillhole TV image. The foliation reflects the dominant regional ENE-WSW strike trend and the mylonitic to ultramylonitic shear zones follow that trend with few exceptions (Fig. 6a). Foliation measured from moderately schistose gneiss represents the regional pervasive background deformation, while the measured mylonitic shear zones occur as <1 mm to up to 42 cm wide localized high-strain zones.

Figure 8a shows the relative intensity of ductile deformation calculated as a moving average for 1 m intervals (THD) as well as the distribution of ductile deformation classes. Despite a heterogeneous distribution of ductile deformation and discrete shear zones, several zones of 1-3 m width with a remarkably regular spacing of 4-6 m (THD) can be observed (Fig. 8a).

4.4 Brittle deformation

In total, 742 fractures have been mapped from the drillhole TV image (Fig. 6b) and 334 from surface mapping. Surface as well as drillhole fracture data show a similar distribution of dominantly ENE-WSW striking, steeply N-dipping fractures with a relatively large scatter spanning almost 90° (n = 502, mean orientation 336/76) and a continuous transition to a more WNW-ESE oriented steep to intermediate NE-dipping fracture orientation. Furthermore, a range of differently oriented fractures can be observed and roughly grouped into three sets: N-S-striking, W-dipping; NW-SE-striking, SW-dipping; and subhorizontal (Fig 6b).

Common brownish staining of fracture surfaces and adjacent host rock material is caused by mineralization of iron(-hydro)-oxides often coating microfractures and impregnating voids within the rock, suggesting fluid circulation through the fracture network under oxidizing conditions.

Kinematic indicators are relatively rare in the study area, mainly due to weathered and lichen-covered outcrop conditions. Furthermore, many of the fractures have only minor offsets not allowing determination of movement directions. Where measurable, there is a tendency for slightly more NE-SW striking sinistral ductile (mostly phyllonitic) shear zones overprinted by more E-W striking brittle dextral faults. Cross-cutting relationships in surface outcrops further corroborate that observation (Fig.

6c). However, as the main fracture set shows a large spread with its mean orientation lying between these two fault type orientations, the sinistral and dextral fracture sets cannot be reliably separated from drillhole TV data.

Approximate position of figure 6

The fracture density (fractures per meter THD) was calculated from the entire drillhole fracture dataset with sampling intervals of 0.5, 1 and 5 m (Fig. 8b). The smallest sampling interval shows a strong fluctuation with maximum values of 44 and minimum values of 2 fractures per m. The 1 m sampling intervals show less fluctuation and vary between 6 fractures per meter and 33 fractures per meter. Generally, the fracture density correlates well with the relative intensity of ductile deformation. The 5 m sampling interval indicates a trend from 10 fractures per meter at the rim of the section to 27 fractures per meter in the vicinity of the central fracture zone with slight fluctuations. However, the general trend of higher fracture density at the central fracture zone is subject to strong fluctuations and does not show a continuous increase. Low fracture density intervals generally correspond to zones of weakly sheared granite while high fracture density occurs mainly near parts of intense ductile deformation and at the boundaries of mylonite zones (e.g. large peaks between 5-6 m THD, 17-20 m THD, 35-36 m THD and 38-39 m THD (Fig. 8ab). However, increased fracture density can also occur where no obvious major ductile preconditioning is present (between 23.8-24.5 m THD) or near zones of core loss (46-47 m THD) (Fig. 8ab). Zones with highest fracture densities accordingly follow the 4-6 m (THD) spacing of the ductile deformation intensity. There appears to be an additional regularly spaced increase in fracture density of ~2 m (THD) (Fig. 8b).

Fracture porosity was calculated from the drillhole TV image using all measurable fractures and their apertures. The representative volume was defined as the cylindrical drillhole in 1 m intervals. Where not measureable, minimum apertures of 0.1 and 0.5 mm were assumed as arbitrary minimum values considering that a certain aperture is needed in order for the fracture to appear on the TV log image because of imaging resolution. For all other fractures, the measured aperture value from the TV log was used to calculate a fracture volume. Of the 742 fractures, 132 had a measurable aperture between

0.8 and 44.8 mm. Calculated fracture volumes within the drillhole accordingly vary between 3.5 and 909.7 cm^3 corresponding to a fracture of 0.5 mm aperture perpendicular to the drillhole and the fracture with the largest aperture of 44.8 mm, respectively. Single fracture volume values were subsequently used for calculating cumulated fracture porosity for 1 m intervals (THD, moving average) along the drilled section (Fig. 8c). In between the intervals, fracture porosity varies between 0.1 and 21.7%, considering the fractures to be void, i.e. without infill. However, drillhole TV images as well as drill core material suggest high-aperture fractures to be filled with fault gouge material and therefore are considered noncohesive breccia zones (Fig. 7). Literature data [*Bossart and Mazurek*, 1991], microporosity analysis (this study) as well as investigation of such a fracture infill suggests a porosity of 10-30%. Values shown in figure 8c represent volumes of fractures per meter drillhole without breccia infill. For subsequent fracture porosity calculations these volumes have been accordingly corrected assuming them to be filled with fault gouge with 10 and 30% porosity (see discussion).

Approximate position of figure 7

Seven larger zones of brecciation have been recognized from the TV imaging that do not show a discrete measurable fracture orientation but have to be considered cataclastic zones between 41.21-41.53 (320 mm aperture), 44.82-44.96 (150 mm aperture), 65.08-65.36 (280 mm aperture), 89.78-90.04 (258 mm aperture), 92.02-92.24 (220 mm aperture; Fig. 7), 92.79-93.13 (340 mm aperture), and 113.35-114.15 (800 mm aperture) meters drilling length. Figure 8c shows the location of these zones along the drillhole, which have been corrected as the aforementioned high-aperture fractures for fracture porosity calculations (see discussion, Table 4 and Fig. 12).

Fracture orientation in 5 m THD intervals are shown in figure 8d. There is only little variation along the drilled section with strong dominance of the ENE-WSW striking steeply dipping main orientation. The NW-SE striking fractures show a difference in dip with a tendency for SW-dipping fractures north of the central fracture zone and more SE-dipping fractures south of it. Fracture intersection lines have been calculated for the same 5 m intervals and show a distribution along a great circle following

the main fracture orientation (Fig. 8e). However, the maxima of the intersection lines show clusters of moderately steep WSW and ENE plunging directions.

Approximate position of figure 8

One key outcrop of this study is located within the deeply incised and steeply descending Totenseebachtal (46°33′41″N 8°20′56″E), which hosts the GBF east of Totensee. While in most places the central section of the GBF is strongly eroded and hidden under Quaternary infill, this outcrop is protected from further erosion and sedimentation by large boulders thereby preserving the to date only known surface outcrop of that section (Fig. 9). It is characterised by an approximately 3 m wide zone of ochre-coloured fault gouge and foliated cataclasites bound by a thin band of the typical hydrothermal breccia on its northern side. Samples for porosity measurements of the central fracture zone where no material could be obtained from the drill core were collected from this outcrop. Fresh fault gouge material preserved within the foliated cataclasite was carefully extracted to retain its internal structure.

Approximate position of figure 9

4.4 Microporosity analysis

Image analysis

Representative samples from all six tectonite groups have been analysed for quantification of microporosity by image analysis and He-pycnometry. Microporosity identified from image analysis was further subdivided into microfractures and matrix porosity (Fig. 10). Microfractures are here defined as fractures crossing the entire analysed thin-section in contrast to the macroscopic fractures used for calculating fracture porosity on the drill core scale, which are defined as structures separating the drill core.

Because of the heterogeneous samples, five different types of matrix porosity have been distinguished, analysed separately and extrapolated for individual thin sections. The different types of

matrix porosity were distinguished according to their dominating mineralogy and texture into i) inter- and intragranular porosity in quartz dominated areas (type 1), ii) solution porosity (i.e. due to albitization and sericitization) of feldspar dominated areas (type 2), iii) inter- and intragranular porosity in fine-grained (average grain size 75 μm, from mylonitic samples) mica dominated areas (type 3), iv) inter- and intragranular porosity in coarse-grained (average grain size 300 μm) mica dominated areas (type 4), and v) breccia porosity, composed of polymineralic clasts (< 1mm in size) surrounded by a fine-grained matrix of ~0.3 μm particle size (type 5). Porosity values for the different matrix porosity types by tectonite vary significantly: Quartz dominated sample areas show a mean porosity of 0.7% with the highest values (1.3%) for the weakly deformed granite sample and the lowest value (0.2%) in the fault breccia. The porosity forms a network along or across single quartz grains with enhanced pore space on the triple points (Fig. 10a). The total matrix porosity is low but appears to be largely interconnected along grain boundaries. Feldspar dominated areas show relatively constant porosity values of between 1.1 and 1.8% (mean 1.4%). Fracturing and subsequent decomposition of the feldspar grains forms porosity networks (Fig. 10b). Fine-grained mica dominated areas show values between 1.9 and 3.4% (mean 2.8%), usually occurring in association with fine-grained (~30 μm) quartz crystals. Although the pores along and across the quartz- and mica grains are very thin, the interconnected porosity network is well developed (Fig. 10c). The coarse-grained mica domains yield higher values between 1.9 and 4.7% (mean 4.6%). Breccia porosity shows significantly higher values between 13.7 and 24.6% (mean 22.0%). The large clasts are mostly fractured and the matrix grains are sometimes packed very tightly, forming zones of reduced porosity. The whole assemblage is further crosscut by microfractures of several μm in width (Fig. 10d). For the extrapolation of the different porosity types to entire thin sections, the mean values have been used (Table 1).

Approximate position of figure 10

Microfractures have been measured and quantified for 10 samples yielding values between 0.8% (ultramylonite) and 5.3% (fault breccia) (Table 1). Values for microfracture porosity within one tectonite group vary significantly and do not show a tectonite specific porosity.

Each thin section has accordingly been divided into the occurring matrix porosity types and the microfractures area and a total 2D porosity was calculated. Areal distribution of the different matrix porosity types over the measured thin sections and different tectonite types as well as the total 2D porosity are given in Table 1.

The weakly deformed granite is dominated by quartz- and feldspar type porosity, while mylonitic and ultramylonitic samples are characterised largely by fine-grained mica-dominated areas. The brittley deformed samples (except GDP09-1) are dominated by breccia porosity (Figure 11).

Approximate position of table 1a&b

He-Pycnometry

The dataset was complemented with porosity calculations on the basis of He-pycnometry data from surface and drill core samples. Twelve surface samples across the outcrop of the central fracture zone (Fig. 9) and 15 samples of the different tectonite types from drill core material were analysed. Sufficient material from the surface samples allowed for 3 subsamples of each sample to be analysed. Because of limited sample material from the drill core, only one analysis per sample was possible. The results from He-pycnometry analysis are summarized in Table 2 and Figure 10.

Porosity of weakly deformed granite varies between 0.1 and 1.5% showing an increase in porosity towards moderately sheared granite with minimum values of 0.6% and maximum calculated porosity of 4.9% for the surface samples and 4.4% for drill core samples. Samples that appear fresh in hand specimen do not show a difference in porosity to those that show a yellowish/brownish staining for the Gr tectonite, whereas non-stained samples of the Gn tectonite show higher porosity than the Gn-s samples (Fig. 11). Mylonite samples vary between 1.8 and 7% total porosity whereas in ultramylonitic samples porosity seems to decrease slightly to 1 to 5.3%. The highest values were measured in cataclastic and fault breccia samples with values up to 9.4% (Table 2, Figure 11).

Approximate position of table 2

4.5 Porosity summary

Comparison of the porosity values for the different tectonites shows a trend of increasing porosity from weakly deformed granite towards mylonite and again a significant decrease for the ultramylonite samples. The highest values of 5-10% (He-pycnometry) and 12-26% (image analysis) are obtained from the cataclasites and fault breccia samples that show an intense brittle overprint. Although the trend is apparent across all applied methods, there is a discrepancy between image analysis and He-pycnometry data for the Gr, Ca and FB samples with over two times higher porosity in the case of image analysis. Several reasons such as (i) preparation artefacts, (ii) sample heterogeneities in the different considered volumes or (iii) physical problems in the case of He-pycnometry can be accounted for, points, which are treated in more detail in the discussion. Mean porosity values calculated from the respective averaged image analysis and He-pycnometry measurements are given in Table 3. These mean porosities have been calculated using the mean He-pycnometry porosity values (Table 2) and the sum of matrix and microfracture porosity from image analysis (Table 1; except for the Gr sample where only the matrix porosity value was used due to overestimation resulting from the large microfractures within that sample).

Approximate position of figure 11

Approximate position of table 3

5 Discussion

This study emphasizes the complexity and multi-scale heterogeneity of repeatedly reactivated fault zones in general and an active hydrothermal system in particular. In the following, the newly obtained structural data and porosity estimations from the Grimsel Breccia Fault are discussed with special focus on the combined effect of fracture networks and enhanced fault-related matrix porosity for long-lived fluid circulation.

5.1 Structural architecture of the GBF

Of the many large-scale (i.e. several meters wide and kilometres long) faults zones clearly recognizable as lineaments of the Grimsel pass shear zone in the wider Grimsel area [*Baumberger*, 2015; *Wehrens et al.*, 2017], the GBF is the only one showing evidence for (palaeo-)hydrothermal activity (Fig. 4), which itself is spatially limited along-strike of the structure and is thus laterally localized on scale of 10s to 100s of meters [*Belgrano et al.*, 2016]. It is one of a series of ENE-WSW striking major shear zones overprinted by brittle fracturing that dissect the Grimsel Pass area. On a large scale, there is no apparent structural distinction between the GBF and the immediately adjacent fault zones in terms of fracture density as reported from tunnel mapping [*Schneider*, 1974] as well as from surface mapping [*Baumberger*, 2015]. The major peculiarities of the GBF are the temperature anomaly related to active hydrothermal outflow [e.g. *Schneider*, 1974; *Pfeifer et al.*, 1992], the formation of a hydrothermally mineralized and multiply reworked hydrothermal breccia [*Stalder*, 1964; *Hofmann et al.*, 2004] and a variably wide and patchy halo of hydrothermal mineralization on fractures surrounding it [*Belgrano et al.*, 2016]. The majority of brittle fractures follows the regional trend of NE-SW to E-W striking structures, an orientation that is consistent across the entire observable range of deformation conditions from dominantly mylonitic deformation under upper greenschist facies (with generally steep lineations) to lower greenschist facies (showing a transition to mainly dextral strike-slip kinematics) to brittle faulting following the earlier established general dextral strike-slip [*Wehrens et al.*, 2017]. Large-scale (several meters wide and several kilometres long) shear zones as well as associated smaller-scale shear zones form an important structural framework for subsequent brittle overprint. Regularly spaced occurrences of increased ductile shear

observed within the drillhole reflects that tight shear zone network and appears to play a key role for localization of increased fracturing (Fig. 8). Drillhole information indicates that brittle deformation intensity in the hydrothermal zone culminates in a central fault core of ~3-5 m width and five subsidiary fault cores north and south of the centre of the fault core characterized by significant zones of cataclastic deformation (Fig. 12). Within the damage zone of the GBF, which encompasses the entire drilled section, many smaller zones (several cm width) of cataclastic material are interconnected by a dense network of low-aperture fractures. The GBF therefore shows a multiple core fault model surrounded by a damage zone several 10s of meters wide [cf. published geometries for the Carboneras Fault and parts of the San Andreas Fault; *Faulkner et al.*, 2003; *Faulkner et al.*, 2010; *Zoback et al.*, 2010]. Field observations in the wider GBF area suggest similar fracture intensities and patterns as well as occasional hydrothermal mineralization extending >100 m either side of the central GBF fracture zone [*Belgrano et al.*, 2016; this study]. In this specific setting, the width of the damage zone appears to exceed the distance between the large-scale faults that can be observed on the surface and which are characterized by a regular increase in fracture density across the tunnel cross-section (Fig. 4). The occurrence of all fracture orientations throughout the observed section as well as widespread hydrothermal mineralization indicates a communicating fracture network along-strike as well as perpendicular to the fault core(s). However, the limited present day extent of the temperature anomaly and focussed outflow of hydrothermal waters is in contrast to the observed extensive fracture network. Furthermore, hydraulic considerations would generally suggest drainage of upwelling fluids at the lowest possible elevation. The observed hydrothermal activity on Grimsel Pass in a position of high elevation and high topographic relief therefore require sealing conditions isolating the GBF hydraulically to the north and south. Such sealing behaviour can partly be explained by the strong anisotropy perpendicular to the GBF caused by the subparallel arrangement of shear zones and, as a function of these, variable fracture density. The smallest matrix porosity values have been measured in the ultramylonitic rocks (Fig. 11). However, the zones with highest ductile deformation intensity are also the zones of highest fracture density, thereby eliminating the sealing properties of the highly sheared rocks. The tightest parts of the GBF have therefore to be considered the zones of weakly ductilely deformed and least fractured granitic host

rock. However, outside of the GBF damage zone the highly anisotropic low-porosity mylonitic and ultramylonitic shear zones often show no brittle reactivation thereby forming sealing structures north and south of the GFB [*Belgrano et al.*, 2016] (Fig. 13).

Approximate position of figures 12 & 13

The prevalence of NE-SW to E-W striking faults results in a preferred clustering of fault intersection lines within the main plane of the GBF. Considering fracture intersections to be zones of enhanced permeability [e.g. *Sibson*, 1996; *Odling et al.*, 2004], porosity might be enhanced along an oblique mesh of tubular intersections within the general orientation of the GBF plane. Channelization of hydrothermal flow through a complex fracture network along the GBF can thus be explained to a certain degree by the anisotropic arrangement of macroscopic fractures.

In the brittle upper part of crystalline basement units the hydraulic conductivity is generally defined by interconnected fracture networks [*Caine et al.*, 1996; *Stober and Bucher*, 2007]. However, while macrofracture porosity has been identified to play an important role for rock permeability under low effective stresses, this effect becomes decreasingly important with increasing effective stress and accordingly increasing depth [e.g. *Walsh*, 1981; *Nara et al.*, 2011]. Mineralization within fractures, fault gouge infill as well as effective stress related closing of fractures can decrease porosity and permeability and in turn enhance the influence of matrix porosity for fluid flow if it can remain open in depth for example due to repeated fracturing during shearing and associated dilatancy. As suggested by Giger et al. [2007 and references therein] there exists a general relationship between porosity and permeability until a certain threshold value. Possible changes in both parameters with increasing P and T are only slightly influenced by geometrical grain rearrangements, but can be strongly affected by hydrothermal mineral precipitation, i.e. by plugging of pore space [*Giger et al.*, 2007]. The investigated breccias of the GBF (Fig. 3b, 5c) show hydrothermal mineral precipitates, which are in parts subsequently overprinted by fracture events. We therefore conclude that the inferred porosity of the breccias will occur also at depth but might be highly dynamic over geological time scales owing to porosity variations in space and time due to fracturing-precipitation cycles.

5.2 Matrix porosity estimations

Quantification of porosity in rocks is a major challenge as possible types of porosity span several orders of magnitude from the nm to cm or even m scale [*Anovitz and Cole*, 2015]. Furthermore, porosity data show a strong method dependency and require a critical evaluation of their validity prior to interpretation [e.g. *Tullborg and Larson*, 2006; *Anovitz and Cole*, 2015; this study].

Mean matrix porosity values of this study lie in the range of 1.3 to 26.18% (image analysis) and 0.9 to 8.3% (He-pycnometry). This relatively large spread can be attributed to artefacts as well as to the chosen representative elemental volume (REV) being too small to counterbalance sample heterogeneity. Despite spread within individual datasets, there is a clear trend of increasing porosity with increasing intensity of ductile deformation from weakly deformed granite to mylonitic overprint. The ultramylonites have slightly lower porosities than the mylonite samples. Porosity measurements from an underground rock laboratory (Grimsel Test Site, GTS) ~3 km NW of the study site, which can be used as a proxy for background porosity values, show an inverse trend ranging from 0.81-1.53% [*Bossart and Mazurek*, 1991]. Their study also shows an increased porosity of up to 2% in ultramylonite affected by brittle deformation. As all sampled rocks of this study lie within the damage zone of the GBF affected by variable but generally intense fracturing, the obtained elevated porosity values are interpreted as an effect of repeated brittle overprint. Although there are significant fluctuations in fracture density and matrix porosity values, which both are functions of the precursor ductile deformation, in the GBF there is no decrease to the background matrix porosity levels (Fig. 12).

Matrix porosity values are dramatically elevated within cataclasites and the fault breccias of the central fracture zone. The central section of the fault core (Fig. 8) could not be directly measured. However, adjacent foliated cataclasites showing small lenses of weakly cemented and therefore cohesive fault gouge were used to extrapolate porosity values to the fault core. Porosity values for fault breccia samples range from 7.5% (He-pycnometry) to 26% (image analysis) and therefore constitute the most porous part of the fault zone (Figs. 12, 13). Fault gouge values estimated on samples from the GTS lie in a comparable range of 10-30% [*Bossart and Mazurek*, 1991].

Several reasons need to be accounted for to explain the discrepancy between He-pycnometry and the image analysis approach: i) larger preparation artefacts owing to plugging out of grains in the weakly cohesive fault gouges with their small grain and pore sizes [*Tullborg and Larson*, 2006]; ii) sample heterogeneities, where the large pycnometer samples average over dense breccia fragments and highly porous matrix, while only high porous domains are considered by image analysis; and (iii) analytical problems in the case of the He-pycnometry technique. To investigate these points, micro-CT analyses on weakly deformed granite and a cohesive fault gouge as two representative end member samples for low and high porosity domains were performed (Fig. 14). The CT image analyses exclude the rim of the sample and therefore preparation artefacts are avoided. For the granite, CT scans reveal the nearly homogenous distribution of small pores over the entire samples volume (Fig. 14c,d). The bulk porosity of 0.1% corresponds well with the values of He-pycnometry (1%) confirming that this approach delivers good estimates for such low porosity samples. In the case of the fault sample, the CT approach yields a pore space of 24%, which is good agreement with the 2D imaging approach but significantly deviates by a factor of 2 from He-pycnometry. Hence, an artificial increase in porosity (i) by sample preparation can be excluded for 2D image analysis. Intriguingly, the gouge CT scan reveals two pore types: interconnected fracture networks and seemingly 'isolated' smaller sized pore patches, where the isolation of the latter might though reflect a resolution problem of the CT scan. Particularly the larger fracture type porosity is heterogeneously distributed, while the smaller isolated pores show a more homogeneous distribution throughout the sample. Sample heterogeneity (ii) might therefore indeed account in parts for aforementioned porosity discrepancy, but (iii) there could also be a problem with the He-pycnometry technique in the case of samples with two different pore type distributions. In the current approach, this problem cannot be solved. Instead of relying on one or the other porosity estimation method, the He-pycnometry data and the image analysis data are used as lower and upper bound values, respectively, over the entire core section (Fig. 12 and discussion below).

Generally, fault gouge material is often described as the lowest porosity part of the fault zone, due to its fine grain size and to mineral cementation, thus it acts a hydraulic barrier [*Caine et al.*, 1996; *Manning and Ingebritsen*, 1999; *Wibberley and Shimamoto*, 2003; *Mitchell and Faulkner*, 2012;

Duan et al., 2017]. The transmissivity of a major fault is largely controlled by the porosity (and related permeability) of fault rock material, which can vary over several orders of magnitude [e.g. *Odling et al.*, 2004]. In the case of the GBF, high porosity fault rock material in the fault core as well as in fracture infill exceeds matrix porosity of solid rock within the damage zone by 2 to 10 times. This can be a result of particle size distribution within the fault rock material and repeated fracturing of the main slip surface in the centre of the GBF impeding sealing by mineral precipitation.

Approximate position of figure 14

5.3 Porosity estimates and their implications for fluid flow

The bulk porosity of the GBF at the meter scale is the sum of rock matrix porosity, fracture density and aperture as well as fracture infill (Fig. 12). While this study yields a relatively wide range of porosity values, it can be shown that the entire zone of the GBF shows elevated porosity values over the studied drillhole section (horizontal distance ~50 m) and presumably beyond (Fig. 12). Elevated fracture porosity values are calculated where fracture density is highest and/or at high-aperture fractures (Fig. 12). However, the main uncertainties in the calculated fracture porosities are due to the unknown apertures of the narrowest fractures (too small to measure) and to the unknown porosity of the fault gouge that fills the fractures. Table 4 shows a comparison of fracture porosity (1 m intervals, THD) using different combinations of apertures of 0.1 and 0.5 mm with fault gouge porosity values of 10 and 30%, respectively. In this case study, it can be shown that the fracture density is of subordinate importance while high-aperture fractures/breccia zones and the porosity of the contained fault gouge have a strong impact on the calculated bulk porosity (Table 4, Fig. 12).

Approximate position of table 4

The bulk permeability of fractures is mainly dependent on the aperture, degree of mineralization, fracture infill and stress acting upon them [*Barton et al.*, 1995]. Especially for the fractures with no measurable aperture, it cannot be reliably defined from drillhole observations. The summed fracture

porosity of the low-aperture fracture network may increase the bulk porosity and permeability of the fault damage zone. Its sensitivity to stress (especially at depth) and clogging by mineral scaling and fine-grained infill could provide an explanation for the isolated and focussed hydrothermal flow along the GBF.

High aperture fractures are comparatively rare and could be considered subsidiary fault cores to the central fracture zone (Fig. 12). These high-aperture fractures occur at previous ductile shear zones indicating reactivated former slip surfaces. Their present-day cataclastic infill suggests that they are also the fault slip surfaces for young brittle movements. It is generally assumed that healing and sealing of fractures and breccias takes place on a short timescale compared to the lifetime of hydrothermal systems [e.g. *Cox*, 2010]. In the case of the GBF such healing can be commonly observed in the well-developed hydrothermal breccia (Fig. 3b), where often mineralization of silica phases dramatically reduced the porosity. On the other hand, many examples of large open pores within the GBF hydrothermal breccia can be observed [*Hofmann et al.*, 2004; *Belgrano et al.*, 2016], suggesting that fluid flow ceased or deviated, thereby preserving these voids. The preservation of the cemented but still porous hydrothermal breccia could therefore be an indication for a shift of the slip zone and the associated fluid flow to the present high-porosity fault slip zones.

5.4 From porosity to permeability

So far, the scale dependency of porosity on the structural architecture of the GBF has been discussed. In order to apply porosities to hydrogeological flow of thermal water, the link to permeability (k), transmissivity (T) and/or hydraulic conductivity (K) needs to be made. The permeability is related to Darcy's law, while transmissivity and/or hydraulic conductivity both depend on time and space intervals within a rock section. In contrast to permeability, transmissivity and hydraulic conductivity can directly be measured in drillholes or on drill-core samples. For a homogeneous pore network, the relation between permeability (k) and conductivity (K) is given by:

$$k = K\frac{\mu}{\rho g}$$

with ρ the density, *g* the earth acceleration and μ the dynamic viscosity of the fluid.

In the case of water (i.e. monophase homogeneous fluid), the values for ρ, g, μ are known and therefore the permeability can directly be derived from the hydraulic conductivity accepting the presence of a homogenous hydrological interval. Resulting estimates give an approximation of water flow rates, but do not include the geometries of the water conducting features of a rock. One can circumvent this drawback by investigating pore geometries and permeabilities independently establishing then a relationship between the two parameters [*e.g. Schild et al.,* 2001, *Giger et al.,* 2007]. Recent studies even investigated pore geometry and permeability simultaneously by in-situ experiments combined with computer tomography [*Wenning,* 2018]. Using experimental approaches always require an intact sampling, i.e. the avoidance of artificial fracturing during sampling/sample preparation or even the disintegration of sample material in the case of fragile and highly fractured material. In this drilling project, unfortunately, the high degree of fracturing did not allow sampling of intact drill core volumes large enough for such experiments. Instead, transmissivities obtained by in situ pumping tests in the drillhole [*Cheng and Renner,* 2018] were evaluated. The transmissivities of Cheng and Renner [2018] were transformed into hydraulic conductivities, assuming a local homogeneous pore structure and flow behaviour within the intervals of the pumping tests yielding values of 10^{-6} to 10^{-7} ms^{-1} (Fig. 15, *Cheng and Renner*, 2018). These values, however, are only representative for domains outside of the core breccia, because drillhole collapse required cement injection in the core domain, impeding drillhole transmissivity measurements in this key structure type. Additionally, hydraulic conductivity data [*Herzog*, 1989, *Schild et al.*, 2001, *Jalali et al.*, 2018, *Wenning et al.*, 2018] from the Nagra Grimsel Test Site (GTS), a rock laboratory situated also in the Aar Massiv plutonic suite nearby (see *Schneeberger et al.*, 2017a, 2018 and references therein), is considered. The GTS area consists of less factured host granitoids compared to the GBF site, which are dissected by faults, along which meteoric water infiltrates very slowly [*Schneeberger et al.*, 2017a,b; 2018]. GTS data provide estimates for background porosity and hydraulic conductivities

outside the GBF for granitoids yielding permeabilities of ~10^{-19} - 10^{-20}m^2 [*Schild et al.*, 2001]. The hydraulic conductivity ranges between 10^{-11} and 10^{-13} ms^{-1} (Fig. 15). These background values are about 4-5 orders of magnitude smaller than those of the fractured rocks in the GBF (Fig. 15). In terms of linking porosity and hydraulic conductivity, an overall increase in the latter from the background host granitoids towards the fractured parts of the GBF can be observed with increasing porosity. Note that fracturing and cataclasis in the GBF result in higher conductivities than those experimentally obtained for quartz gouges [*Giger et al.*, 2007; Fig. 15]. Owing to aforementioned reasons, unfortunately, no hydraulic conductivities for the core breccia of GBF are available, leaving room for speculation within a range of possible values. Taking the estimated core breccia porosities of 10-30 vol% (Figs. 11, 12) and extrapolating the conductivity-porosity trend of Figure 15, suggests at least equal values of 10^{-6} to 10^{-7} ms^{-1} compared to the fractured part, most likely even higher values. In fact, unconsolidated densely packed sands vary around 10^{-5} to 10^{-2} ms^{-1} and may represent the upper bound of the expected hydraulic conductivity range. Hence, directly after a rupturing event such high hydraulic conductivites might be considered for deep circulating hydrothermal fluids for an unclogged stage of the GBF. These high hydraulic conductivites may reduce over time as a consequence of ongoing cementation and clogging.

Approximate position of figure 15

5.5 *Large-scale fluid circulation*

Although the GBF shows hydrothermal mineralization, which documents up-flow of warm water, enhanced hydrothermal mineralization is patchy along the entire length of the fault and mainly observed in two zones (the Sidelhorn linkage zone and the Grimsel Pass-Gletsch damage zone that has been drilled for this study [*Belgrano et al.*, 2016] (Fig. 13). Dilatancy within fault linkages can be considered a major fault intersection zone forming potential tubular volumes of high permeability, possibly corresponding to ‘implosion breccias’ within dilatational fault jogs as defined by [*Sibson*, 1986]. Extensive up-flow within a damage zone along the straight part of the GBF, however, lacks such a straight-forward explanation. The combination of fracture and matrix porosity data from this study shows an elevated porosity for the entire damage zone that exceeds the background porosity of

granitoids in the Aar Massif [cf. *Bossart and Mazurek*, 1991, Fig. 15]. However, although hydrothermal mineralization over several 10s of meters on either side of the central fracture zone indicates penetration of hydrothermal fluids far through the damage zone [*Belgrano et al.*, 2016], the focussed present-day exfiltration of hydrothermal waters and its associated thermal anomaly is centred on the fault core. The damage zone is therefore interpreted to have a high potential for fluid transmissivity but is not sustained, possibly due to rapid mineralization of factures and/or stress related closure. The offset between present-day exfiltration of hydrothermal water in the Transitgas AG tunnel and the mapped extent of hydrothermal mineralization could be an effect of such changing fluid pathways across the damage zone (Fig. 2). Furthermore, different inflow points in the tunnel have been reported, possibly indicating such short-timescale fluctuations of fluid flow in the damage zone [*Schneider*, 1974; *Pfeifer et al.*, 1992; *Hofmann et al.*, 2004; *Belgrano et al.*, 2016]. The fault core(s) on the other hand retain constant high permeability due to repeated fracturing and breccia formation possibly associated with seismic activity [cf. *Sibson*, 1987; *Micklethwaite and Cox*, 2004] (Fig. 13). However, the measured maximum porosity values could represent a specific situation of a dynamic porosity distribution in the fault core. Episodic fracturing, hydrothermal cementation and reorganisation of gouge material associated to fault movement might change the bulk porosity dramatically with time [e.g. *Micklethwaite and Cox*, 2004; *Micklethwaite et al.*, 2015]. In that sense, the present day near-surface porosity might represent an analogue to dynamic open porosity at depth, which episodically decreases and reopens, while at the near-surface closing of pore space does not take place anymore and open porosity is therefore preserved. This could further lead to a hydraulic gradient guiding hydrothermal water along the fault core. However, the present deep circulation of fluids despite the lack of active movement along the GBF indicates certain interseismic open fluid pathways.

A possible explanation for the elevated patchy hydrothermal mineralization on Grimsel Pass could lie in the fault-intersection distribution. Structural geometries on geology are often fractal, with patterns and anisotropies observed in small scale (e.g. in outcrop) being self-similar across scales [e.g. *Barton and Zoback*, 1992]. Clustering of fault intersections calculated from drillhole data (Fig. 8) interpreted

as zones of enhanced permeability could therefore explain the Grimsel Pass hydrothermal zone as the intersection of such a large-scale intersection mesh along the plane of the GBF with the surface. Because the topography falls away to the north and south of Grimsel Pass, infiltration of meteoric water into the GBF can only occur in the elevated areas along strike to the west of Grimsel Pass. In the recharge area the damage zone around the GBF could funnel water through the dense but presumably narrowing downward fracture network towards the centre of the GBF, feeding the hydrothermal reservoir. In that sense, the entire length of the GBF and the associated damage zone could be water-saturated by infiltrating waters, while up-flow of hydrothermal waters is strongly focussed in the main and subsidiary fault cores filled with highly permeable fault rocks in the direction of increased fault intersection (Fig. 13).

6 Conclusions

The unique opportunity to sample a continuous section of rock material and structural data across the Grimsel Breccia Fault active hydrothermal zone in the high Swiss Alps provides insight into the processes leading to the sustained water circulation along hydrothermally active faults. We have established a critical correlation between the tectonic preconditioning of a fault zone during its evolution from ductile shear zone to brittle fault (and thus its uplift and exhumation) and its bulk porosity. The intensity of ductile strain is of key importance for the matrix porosity of the host rock as well as for localization of the subsequent brittle overprint. Matrix porosity over the entire studied zone shows elevated values compared to true background porosity measured in intact rocks of the Grimsel test site. We observe the highest porosity in zones with repeated fracturing, slip and highest accumulation of strain inducing the formation of fault gouges. Bulk porosity along the GBF is very sensitive to large-scale fractures and the related fault gouge porosity, in contrast to faults with fine-grained and clay-rich fault gouge cores often observed in other settings.

As a great advantage, the fine-grained domains allow for an efficient heat exchange between solid rock and circulating fluid as transport medium. The study area in the Aar Massif as one of the external crystalline massifs of the Swiss Alps can therefore be used as an analogue to the crystalline basement below the northern Alpine foreland basin, where key target areas for future geothermal exploration

projects are situated at 4-5 km depth but also as proxy for potentially exploitable orogenic hydrothermal systems. The close link between ductile preconditioning of the host rock for its susceptibility for brittle fracturing and the development and preservation of related fluid pathways emphasizes the importance of detailed understanding of the long-term tectonic history of a target area for successful exploration and ultimately exploitation of geothermal energy.

Acknowledgments

This project is part of the NRP70 program and is funded by the Swiss National Science Foundation (grant number: SNF-153889). It was carried out within the framework of the Swiss Competence Center for Energy Research – Supply of Energy (SCCER-SoE). We thank Ch. Wibberley and one anonymous reviewer for constructive reviews and P. Agard (Editor-in-Chief, Tectonophysics) for the support and manuscript handling. Stefan Lustenberger is thanked for helping with temperature measurements and structural analysis of the Transitgas AG tunnel section as well as U. Mäder and N. Waber for helpful discussions. We further thank Swisstopo, the Swiss Federal Office of Energy, NAGRA and the Kraftwerke Oberhasli AG for additional financial and practical support.

Figure captions:

Figure 1. Geologic map of the central Aar Massif, modified after [Berger et al., 2016]. Mapped extent of hydrothermal mineralisation as well as the trace of cross-section (Fig. 4) is shown.

Figure 2. Shear zone and fault structures in the Grimsel area. (a) Ductile shear zones and Grimsel Breccia Fault with hydrothermal mineralisation indicating domain of paleo-hydrothermal flow [after Belgrano et al., 2016]. For lithologies see legend of figure 1. (b) Aerial image (Source: Federal Office of Topography swisstopo; reproduced by permission of swisstopo (BA17136)) of the Grimsel Pass hydrothermal zone showing the extent of mineralized outcrops [after Belgrano et al., 2016], trace of the drillhole, presumed trace of the GBF core and the surface projection of the Transitgas AG tunnel (with the interval of active hydrothermal inflow of 18-28°C, white stippled line).

Figure 3. a) Morphological expression of the Grimsel Breccia Fault at the drill site, b) mineralized hydrothermal breccia from the core of the GBF. Clasts consist of weakly deformed to mylonitic metagranite of <cm to several cm size and are cemented by microcrystalline quartz, sulphides and Fe-(hydr-)oxides (46°33’40’’N, 8°20’51’’E), c) chalcedony-mineralized fractures embedded in weakly deformed granite at ~20 m horizontal distance north of the GBF (46°33′39″N, 8°20′40″E)

Figure 4. a) Geologic cross-section along the Transitgas AG tunnel below Grimsel Pass showing the drillhole (projected into the section), rock-wall temperatures and main ductile shear zones. b) Fracture density along the cross-section correlates mostly with ductile shear zones but only one fracture zone correlates with enhanced tunnel temperatures. c) Lower hemisphere equal-area pole plots (2% contour interval) of mapped fractures in the tunnel reflecting, with few exceptions, the general dominating WNW-ESE strike.

Figure 5. a) Overview of the drillhole GDP-1 showing the intersection with the central fracture zone, the ductile deformation intensity, zones of core loss and brecciation, sample locations and location for images b-e., b) example from the drillcore showing heterogeneous ductile deformation on a small scale as well as yellowish staining, c) drill core sample of the hydrothermal breccia, d) TV image of

open fracture adjacent to brecciated zone, and e) TV image of open fracture surrounded by weakly deformed granite.

Figure 6. a) Main foliation and shear zone orientation of the drillhole measured from TV imaging, b) fractures measured from TV imaging, and c) overprinting relationship in a surface outcrop of weakly deformed granite showing dextral and sinistral shear fractures with small intersection angles both lying within the spread of the main orientation.

Figure 7. TV image and drillcore example of a single high-aperture fracture filled with breccia material embedded in mylonitic host-rock. The TV image shows that part of the fracture infill was washed out during drilling resulting in open space, which is not the case for the preserved infill visible in the core material.

Figure 8. Structural summary of the drillhole GDP-1: a) relative ductile deformation intensity inferred from core mapping, b) fracture density as moving average with 0.5, 1 and 5 m sampling intervals, c) moving average (1 m sampling interval) of fracture volumes observed in the drillhole assuming the fractures to be 100% void. Black bars indicate larger breccia zones and major core loss, d) contoured lower-hemisphere pole plots of fractures for 5 m (THD) intervals, and e) contoured lower-hemisphere plots of fracture intersection lines.

Figure 9. Surface appearance of the central fracture zone (46°33′41″N, 8°20′56″E). Sample points for porosity measurements are indicated. The walls of the fault zone consist of moderately schistose gneiss in this outcrop.

Figure 10. Examples of the distinguished porosity types: a) Microphotograph taken under cross-polarized and UV light showing tight quartz minerals and intragranular (green) porosity between grains (A), b) electron backscatter (BE) image of partly decomposed feldspar showing alteration (A), solution porosity (B) and microfractures (C), c) electron backscatter image of a mica dominated domain with preparation related large fractures (A) and typical porosity at mica sheet boundaries (B), d) electron backscatter image of a typical fault breccia porosity with zones of variable fragment size and accordingly variably porous matrix (A & B). Porosity in BE images (b-c) are black.

Figure 11. (Upper row) Porosity data from the different methods for quantification of matrix- and microfracture-porosity as well as images of polished hand specimens (lower row) showing the typical appearance of the analysed tectonite types (image height is 2 cm). See text for details.

Figure 12. a) Variation of matrix porosity across the GBF using mean matrix porosity values of the ductile tectonite types given in table 3 (moving average, 1 m sampling interval), b) Variation of minimum and maximum fracture porosity values across the GBF (moving average, 1 m sampling interval), c) Sum of matrix and fracture porosity, i.e. bulk porosity, across the GBF shows the dominating influence of fault gouge filled high-aperture fractures and larger breccia zones for the overall porosity distribution.

Figure 13. Schematic block-diagrams showing the proposed porosity distribution on a) the km scale showing the two main upflow zones, b) the 10 m scale including the damage zone and the fault core, and c) the micrometre scale within the hydrothermal breccia.

Figure 14. 3D distribution of porosity from CT scans. (a+c) Greyscale 3D image of the scanned sample; (b+d) thresholded values of the porosity showed as coloured volumes. (a+b) relative intact granitic gneiss, 3D porosity estimate at this resolution ~1 vol%; (c+d) gouge breccia sample: porosity 24 vol%. Note the similar distribution of the porosity in different sectional planes and the irregular cutting effects of the pores in 3D allowing a certain transmissivity.

Figure 15. Compilation of literature data showing the relationship between porosity and hydraulic conductivity for the Aar Massif in general and the Grimsel Breccia Fault. In addition, experimental data from quartz fault gouges from Giger et al. 2007 are shown for comparison. The ductily deformed and granitoid parts are given from laboratory measurements of cores by Schild et al. (2001) and Wenning et al. (2018). These data-sets include also measured porosities. For comparison conductivity data from pumping tests in the same locations are included (Jalali et al. 2018).

References:

Abrecht, J. (1994), Geologic units of the Aar massif and their pre-Alpine rock associations: a critical review : the pre-Alpine crustal evolution of the Aar-, Gotthard- and Tavetsch massifs, *Schweizerische mineralogische und petrographische Mitteilungen*, *74*(1), 5-27.

Allmendinger, R. W. (2016), Stereonet 9.5 User Manual, 45.

Allmendinger, R. W., N. C. Cardozo, and D. E. Fisher (2012), *Structural Geology Algorithms: Vectors & Tensors*, Cambridge University Press, Cambridge.

Anovitz, L. M., and D. R. Cole (2015), Characterization and Analysis of Porosity and Pore Structures, *Reviews in Mineralogy and Geochemistry*, *80*(1), 61-164.

Barton, C. A., and M. D. Zoback (1992), Self-similar distribution and properties of macroscopic fractures at depth in crystalline rock in the Cajon Pass Scientific Drill Hole, *Journal of Geophysical Research: Solid Earth*, *97*(B4), 5181-5200.

Barton, C. A., M. D. Zoback, and D. Moos (1995), Fluid flow along potentially active faults in crystalline rock, *Geology*, *23*(8), 683-686.

Baumberger, R. (2015), Quantification of Lineaments: Link between internal 3D structure and surface evolution of the Hasli valley (Aar massif, central alps, Switzerland). PhD Thesis, University of Bern.

Belgrano, T. M., M. Herwegh, and A. Berger (2016), Inherited structural controls on fault geometry, architecture and hydrothermal activity: an example from Grimsel Pass, Switzerland, *Swiss Journal of Geosciences*, 1-20.

Bergemann, C., E. Gnos, A. Berger, M. Whitehouse, J. Mullis, P. Wehrens, T. Pettke, and E. Janots (2017), Th-Pb ion probe dating of zoned hydrothermal monazite and its implications for repeated shear zone activity: An example from the Central Alps, Switzerland, *Tectonics*, *36*(4), 671-689.

Berger, A., I. Mercolli, and E. Gnos (2016), Geological map of the Aar Massif, Tavetsch and Gotthard nappes 1:100000, Landesgeologie der Schweiz.

Berger, A., P. Wehrens, P. Lanari, H. Zwingmann, and M. Herwegh (2017), Microstructures, mineral chemistry and geochronology of white micas along a retrograde evolution: An example from the Aar massif (Central Alps, Switzerland), *Tectonophysics*, *721*, 179-195.

Bianchetti, G., P. Roth, F.-D. Vuataz, and J. Vergain (1992), Deep groundwater circulation in the Alps: Relations between water infiltration, induced seismicity and thermal springs. The case of Val d'Illiez, Wallis, Switzerland, *Eclogae Geologicae Helvetiae*, *85*(2), 291-305.

Bossart, P., and M. Mazurek (1991), Structural geology and water flow-paths in the migration shear-zone*Rep.*, 66 pp.

Caine, J. S., J. P. Evans, and C. B. Forster (1996), Fault zone architecture and permeability structure, *Geology*, *24*(11), 1025-1028.

Challandes, N., D. Marquer, and I. Villa (2008), P-T-t modelling, fluid circulation, and 39Ar-40Ar and Rb-Sr mica ages in the Aar Massif shear zones (Swiss Alps), *Swiss Journal of Geosciences*, *101*(2), 269-288.

Cheng, Y., and J. Renner (2017), Exploratory use of periodic pumping tests for hydraulic characterization of faults, *Geophysical Journal International, 212*, 543-565.

Choukroune, P., and D. Gapais (1983), Strain pattern in the Aar Granite (Central Alps): Orthogneiss developed by bulk inhomogeneous flattening, *Journal of Structural Geology*, *5*(3), 411-418.

Cox, S. F. (2010), The application of failure mode diagrams for exploring the roles of fluid pressure and stress states in controlling styles of fracture-controlled permeability enhancement in faults and shear zones, *Geofluids*, *10*(1-2), 217-233.

Duan, Q., X. Yang, and J. Chen (2017), Hydraulic properties of a low permeable rupture zone on the Yingxiu-Beichuan Fault activated during the Wenchuan earthquake, China: Implications for fluid conduction, fault sealing, and dynamic weakening mechanisms, *Tectonophysics*, *721*(Supplement C), 123-142.

Evans, J. P., C. B. Forster, and J. V. Goddard (1997), Permeability of fault-related rocks, and implications for hydraulic structure of fault zones, *Journal of Structural Geology*, *19*(11), 1393-1404.

Faulkner, D. R., A. C. Lewis, and E. H. Rutter (2003), On the internal structure and mechanics of large strike-slip fault zones: field observations of the Carboneras fault in southeastern Spain, *Tectonophysics*, *367*(3), 235-251.

Faulkner, D. R., C. A. L. Jackson, R. J. Lunn, R. W. Schlische, Z. K. Shipton, C. A. J. Wibberley, and M. O. Withjack (2010), A review of recent developments concerning the structure, mechanics and fluid flow properties of fault zones, *Journal of Structural Geology*, *32*(11), 1557-1575.

Fridleifsson, I. B., R. Bertani, E. Huenges, J. W. Lund, A. Ragnarsson, and L. Rybach (2008), The possible role and contribution of geothermal energy to the mitigation of climate change, in *IPCC scoping meeting on renewable energy sources : Proceedings*, edited by O. Hohmeyer and T. Trittin, pp. 59-80, Intergovernmental Panel on Climate Change.

Frieg, B., W. R. Alexander, H. Dollinger, C. Bühler, P. Haag, A. Möri, and K. Ota (1998), In situ resin impregnation for investigating radionuclide retardation in fractured repository host rocks, *Journal of Contaminant Hydrology*, *35*(1), 115-130.

Giger, S. B., E. Tenthorey, S. F. Cox, and J. D. Fitz Gerald (2007), Permeability evolution in quartz fault gouges under hydrothermal conditions, *Journal of Geophysical Research: Solid Earth*, *112*(B7).

Goncalves, P., E. Oliot, D. Marquer, and J. A. D. Connolly (2012), Role of chemical processes on shear zone formation: an example from the Grimsel metagranodiorite (Aar massif, Central Alps), *Journal of Metamorphic Geology*, *30*(7), 703-722.

Häring, M. O., U. Schanz, F. Ladner, and B. C. Dyer (2008), Characterisation of the Basel 1 enhanced geothermal system, *Geothermics*, *37*(5), 469-495.

Herzog, F. (1989), Hydrologic modelling of the migration site at the Grimsel Test Site - the steady state. *Technical Report 89-16*, NAGRA.

Heilbronner, R., and N. Keulen (2006), Grain size and grain shape analysis of fault rocks, *Tectonophysics*, *427*(1), 199-216.

Heilbronner, R., and S. Barrett (2013), *Image Analysis in Earth Sciences*, Springer Verlag, Heidelberg.

Herwegh, M., A. Berger, R. Baumberger, P. Wehrens, and E. Kissling (2017), Large-Scale Crustal-Block-Extrusion During Late Alpine Collision, *Scientific Reports*, *7*(1), 413.

Hofmann, B. A., M. Helfer, L. W. Diamond, I. M. Villa, R. Frei, and J. Eikenberg (2004), Topography-driven hydrothermal breccia mineralization of Pliocene age at Grimsel Pass, Aar massif, Central Swiss Alps, *Schweizerische mineralogische und petrographische Mitteilungen*, *84*(3), 271-302.

Jalali, M., Gischig, V., Doetsch, J., Näf, R., Krietsch, H., Klepikova, M., Amann, F. and D. Giardini (2018). Transmissivity changes and microseismicity induced by small-scale hydraulic fracturing tests in crystalline rock. *Geophysical Research Letters, 45*, 2265–2273.

Kralik, M., N. Clauer, R. Holnsteiner, H. Huemer, and F. Kappel (1992), Recurrent fault activity in the Grimsel Test Site (GTS, Switzerland): revealed by Rb-Sr, K-Ar and tritium isotope techniques, *Journal of the Geological Society*, *149*(2), 293-301.

Manning, C. E., and S. E. Ingebritsen (1999), Permeability of the continental crust: Implications of geothermal data and metamorphic systems, *Rev. Geophys.*, *37*(1), 127-150.

Marrett, R., and R. W. Allmendinger (1990), Kinematic analysis of fault-slip data, *Journal of Structural Geology*, *12*(8), 973-986.

Martinez-Landa, L., and J. Carrera (2005), An analysis of hydraulic conductivity scale effects in granite (Full-scale Engineered Barrier Experiment (FEBEX), Grimsel, Switzerland), *Water Resources Research*, *41*(3), n/a-n/a.

Michalski, I., and M. Soom (1990), The Alpine thermo-tectonic evolution of the Aar and Gotthard massifs, Central Switzerland : fission track ages on zircon and apatite and K-Ar mica ages, *Schweizerische mineralogische und petrographische Mitteilungen*, *70*, 373-387.

Micklethwaite, S., and S. F. Cox (2004), Fault-segment rupture, aftershock-zone fluid flow, and mineralization, *Geology*, *32*(9), 813-816.

Micklethwaite, S., A. Ford, W. Witt, and H. A. Sheldon (2015), The where and how of faults, fluids and permeability – insights from fault stepovers, scaling properties and gold mineralisation, *Geofluids*, *15*(1-2), 240-251.

Mitchell, T. M., and D. R. Faulkner (2009), The nature and origin of off-fault damage surrounding strike-slip fault zones with a wide range of displacements: A field study from the Atacama fault system, northern Chile, *Journal of Structural Geology*, *31*(8), 802-816.

Mitchell, T. M., and D. R. Faulkner (2012), Towards quantifying the matrix permeability of fault damage zones in low porosity rocks, *Earth and Planetary Science Letters*, *339*, 24-31.

Nara, Y., P. G. Meredith, T. Yoneda, and K. Kaneko (2011), Influence of macro-fractures and micro-fractures on permeability and elastic wave velocities in basalt at elevated pressure, *Tectonophysics*, *503*(1), 52-59.

Odling, N. E., S. D. Harris, and R. J. Knipe (2004), Permeability scaling properties of fault damage zones in siliclastic rocks, *Journal of Structural Geology*, *26*(9), 1727-1747.

Pfeifer, H.-R., A. Sanchez, and C. Degueldre (1992), Thermal springs in granitic rocks from the Grimsel Pass (Swiss Alps): The late stage of a hydrothermal system related to Alpine Orogeny, in *Water-Rock Interaction*, edited by S.-G. o. W.-R. I. E. International Association of Geochemistry and Cosmochemistry and Alberta Research Council, AB, International, pp. 1327-1331, Rotterdam.

Pfiffner, O. A., P. Erard, and M. Stäuble (1997), Two cross sections through the Swiss Molasse Basin (lines E4 – E6, W1, W7– W10), in *Deep Structure of the Swiss Alps: Results of NRP 20*, edited by O. A. Pfiffner, P. Lehner, P. Heitzmann, S. Mueller and A. Steck, pp. 64-72, Birkhäuser, Basel, Switzerland.

Pleuger, J., N. Mancktelow, H. Zwingmann, and M. Manser (2012), K–Ar dating of synkinematic clay gouges from Neoalpine faults of the Central, Western and Eastern Alps, *Tectonophysics*, *550-553*, 1-16.

Rolland, Y., S. F. Cox, and M. Corsini (2009), Constraining deformation stages in brittle–ductile shear zones from combined field mapping and 40Ar/39Ar dating: The structural evolution of the Grimsel Pass area (Aar Massif, Swiss Alps), *Journal of Structural Geology*, *31*(11), 1377-1394.

Schaltegger, U. (1990), Post-magmatic resetting of Rb-Sr whole rock ages — a study in the Central Aar Granite (Central Alps, Switzerland), *Geologische Rundschau*, *79*(3), 709-724.

Schaltegger, U., and F. Corfu (1992), The age and source of late Hercynian magmatism in the central Alps: evidence from precise U−Pb ages and initial Hf isotopes, *Contributions to Mineralogy and Petrology*, *111*(3), 329-344.

Schild, M., S. Siegesmund, A. Vollbrecht, and M. Mazurek (2001), Characterization of granite matrix porosity and pore-space geometry by in situ and laboratory methods, *Geophysical Journal International*, *146*(1), 111-125.

Schindelin, J., C. T. Rueden, M. C. Hiner, and K. W. Eliceiri (2015), The ImageJ ecosystem: An open platform for biomedical image analysis, *Molecular Reproduction and Development*, *82*(7-8), 518-529.

Schneeberger, R., de La Varga, M., Egli, D., Berger, A., Kober, F., Wellmann, F., and M. Herwegh, (2017a). Methods and uncertainty estimations of 3-D structural modelling in crystalline rocks: a case study. *Solid Earth, 8,* 987-1002.

Schneeberger, R., Maeder, U.K., and H.N. Waber (2017b). Hydrochemical and isotopic (delta2H, delta18O, 3H) characterization of fracture water in crystalline rock (Grimsel, Switzerland). *Procedia Earth and Planetary Science, 17*, 738-741.

Schneeberger, R., Egli, D., Lanyon, G.W., Mäder, U.K., Berger, A., Kober, F. and M. Herwegh (2018). Structural-permeability favorability in crystalline rocks and implications for groundwater flow paths: a case study from the Aar Massif (central Switzerland). *Hydrogeology Journal,* 1-14.

Schneider, C. A., W. S. Rasband, and K. W. Eliceiri (2012), NIH Image to ImageJ: 25 years of image analysis, *Nat Meth*, *9*(7), 671-675.

Schneider, T. R. (1974), Geologische Stollenaufnahmen Transitgas AG: Unterstock-, Urweid-, Gstelli-, Grimsel- und Obergesteln Stollen*Rep.*, Elektro-Watt Ingenieurunternehmung AG, Zürich.

Sibson, R. H. (1986), Brecciation processes in fault zones: Inferences from earthquake rupturing, *Pure and Applied Geophysics*, *124*(1), 159-175.

Sibson, R. H. (1987), Earthquake rupturing as a mineralizing agent in hydrothermal systems, *Geology*, *15*(8), 701-704.

Sibson, R. H. (1996), Structural permeability of fluid-driven fault-fracture meshes, *Journal of Structural Geology*, *18*(8), 1031-1042.

Sonney, R., and F.-D. Vuataz (2008), Properties of geothermal fluids in Switzerland: A new interactive database, *Geothermics*, *37*(5), 496-509.

Sonney, R., and F.-D. Vuataz (2009), Numerical modelling of Alpine deep flow systems: a management and prediction tool for an exploited geothermal reservoir (Lavey-les-Bains, Switzerland), *Hydrogeology Journal*, *17*(3), 601-616.

Stalder, H. A. (1964), Petrographische und mineralogische Untersuchungen im Grimselgebiet, *Schweizerische mineralogische und petrographische Mitteilungen*, *44*, 187-398.

Steck, A. (1968), Die alpidischen Strukturen in den Zentralen Aaregraniten des westlichen Aarmassivs, *Eclogae Geologicae Helvetiae*, *61*(1), 19-48.

Stober, I., and K. Bucher (2007), Hydraulic properties of the crystalline basement, *Hydrogeology Journal*, *15*(2), 213-224.

Tullborg, E.-L., and S. A. Larson (2006), Porosity in crystalline rocks – A matter of scale, *Engineering Geology*, *84*, 75-83.

Viana, M., P. Jouannin, C. Pontier, and D. Chulia (2002), About pycnometric density measurements, *Talanta*, *57*(3), 583-593.

Waber, H. N., R. Schneeberger, U. K. Mäder, and C. Wanner (2017), Constraints on Evolution and Residence time of Geothermal Water in Granitic Rocks at Grimsel (Switzerland), *Procedia Earth and Planetary Science*, *17*, 774-777.

Walsh, J. B. (1981), Effect of pore pressure and confining pressure on fracture permeability, *International Journal of Rock Mechanics and Mining Sciences & Geomechanics Abstracts*, *18*(5), 429-435.

Wehrens, P., R. Baumberger, A. Berger, and M. Herwegh (2017), How is strain localized in a meta-granitoid, mid-crustal basement section? Spatial distribution of deformation in the central Aar massif (Switzerland), *Journal of Structural Geology*, *94*, 47-67.

Wehrens, P., A. Berger, M. Peters, T. Spillmann, and M. Herwegh (2016), Deformation at the frictional-viscous transition: Evidence for cycles of fluid-assisted embrittlement and ductile deformation in the granitoid crust, *Tectonophysics*, *693, Part A*, 66-84.

Wenning, Q.C., 2018. Investigating petrophysical properties of reservoir rocks using traditional and computerized tomography techniques. Unpublished PhD Thesis, ETH Zürich, Switzerland.

Wenning, Q.C., Madonna, C., de Haller, A., and J.-P. Burg, (2018). Permeability and seismic velocity anisotropy across a ductile-brittle fault zone in crystalline rock. *Solid Earth, 9, 683-698*.

Wibberley, C. A. J., and T. Shimamoto (2003), Internal structure and permeability of major strike-slip fault zones: the Median Tectonic Line in Mie Prefecture, Southwest Japan, *Journal of Structural Geology*, *25*, 59-78.

Wibberley, C. A. J., G. Yielding, and G. Di Toro (2008), Recent advances in the understanding of fault zone internal structure: a review, *Geological Society, London, Special Publications*, *299*(1), 5-33.

Zoback, M. L., S. Hickman, and W. Ellsworth (2010), Scientific Drilling Into the San Andreas Fault Zone, *Eos, Transactions American Geophysical Union*, *91*(22), 197-199.

		matrix porosity (SEM analysis)						UV microscopy	Total porosity [%]
Rock type	**Sample**	**Type 1 [%]**	**Type 2 [%]**	**Type 3 [%]**	**Type 4 [%]**	**Type 5 [%]**	**Total matrix porosity [%]**	**microfractures [%]**	
Granite	GDP13	29	62	-	4	-	1	5	6
Mylonite	GDP18	32	32	34	-	-	2	2	4
Mylonite	GDP12	10	73	13	-	-	1	4	6
Ultra-mylonite	RL01	25	10	63	-	-	2	2	4
Ultra-mylonite	RL04	22	59	18	-	-	2	1	2
Cataclasite	Gu07	57	-	-	-	40	9	3	12
Cataclasite	GDP09-1	-	-	47	-	49	12	4	16
Fault breccia	GDP11-2	46	-	-	6	43	10	5	15
Fault breccia	GDP09-2	-	-	-	-	95	21	5	26
Fault breccia	GDP02-1	-	-	-	-	98	22	2	24

Table 1a. Matrix porosity types and microfractures in relation to entire thin sections analysed by image analysis. The sum of the matrix porosity types (in area% relative to the entire thin section) and the microfractures analysed based on UV microscopy (in area%) add to 100%.

Matrix type	**Average porosity [%]**	**Number of analysis**	**Average size of individual analysed area**	**Deviation between areas [%]**
Type 1-matrix	0.7	6	~0.4 mm^2	0.5
Type 2-matrix	1.4	6	~0.4 mm^2	0.3
Type 3-matrix	2.8	3	~0.4 mm^2	0.8
Type 4-matrix	4.6	3	~0.4 mm^2	1.6
Type 5-matrix	22.0	5	~0.4 mm^2	4
microfractures	-	10 samples	~8 cm^2	

Table 1b. Individual results from image analysis, which are used as input for the cascade calculation presented in Table 1a. First order error-estimations depend on the amount of matrix type in the cascade (samples with high proportions of matrix type 4 and 5 have larger error as samples dominated by matrix type 1 and 2.

Rock type	Number		Measured volumes [cm3]	He-Pycnometry porosity [%]		
	Drill-hole	Surface		min.	max.	mean
Granite	4	-	2.0 – 3.4	0.1	1.5	0.9
Gneiss	4	3	2.4 – 3.0	0.6	4.9	2.6
Mylonite	4	1	2.4 – 2.9	1.8	7	4.4
Ultra-mylonite	2	1	2.7 – 2.8	1	5.3	3
Cataclasite	-	5	2.5 – 3.3	6	8.4	7.6
Fault breccia	-	2	2.4 – 2.8	7.5	9.4	8.3

Table 2. He-pycnometry data from drill core and surface samples including measured volumes, connected and total porosity.

Rock type	Number of samples		Porosity [%]		
	Image analysis	He-pycnometry	min.	max.	**mean**
Granite	1	4	0.1	1.5	**0.9**
Gneiss	-	7	0.6	4.4	**2.3**
Mylonite	2	5	1.8	5.9	**4.0**
Ultra-mylonite	2	3	1.0	5.3	**3.0**
Cataclasite	2	5	6.0	16.5	**10.8**
Fault breccia	3	2	8.0	26.2	**14.8**

Table 3. Mean porosity values of the different tectonite groups based on image analysis and He-pycnometry.

	Assumed aperture	Assumed fault gouge porosity	Calculated porosity for low fracture density [%]			Calculated porosity for medium fracture density [%]			Calculated porosity for high fracture density [%]		
Fracture density range			6 - 8 fracs./m			15 - 16 fracs./m			30 - 32 fracs./m		
Number of intervals			n = 14			n = 21			n = 8		
			min.	max.	**mean**	min.	max.	**mean**	min.	max.	**mean**
Min. estimate	0.1 mm	10%	0.01	0.22	**0.09**	0.08	1.83	**0.43**	0.37	1.43	**0.65**
	0.5 mm	10%	0.07	0.27	**0.14**	0.18	1.95	**0.52**	0.54	1.61	**0.83**
	0.1 mm	30%	0.04	0.66	**0.26**	0.25	5.49	**1.28**	1.11	4.28	**1.96**
Max. estimate	0.5 mm	30%	0.2	0.81	**0.42**	0.54	5.84	**1.55**	1.63	4.82	**2.49**

Table 4. Examples of calculated fracture porosity using assumed minimum and maximum values for an assumed minimum aperture and fault gouge porosity.

Highlights:

- A continuous bulk porosity profile across a fault zone is presented
- Bulk porosity is controlled by the fracture network and its fault gouge infill
- Recent thermal fluid flow is located at locations of combined high fracture- and matrix porosity
- Repeated fracturing is necessary to keep a hydrothermal system running for a long time (ma)

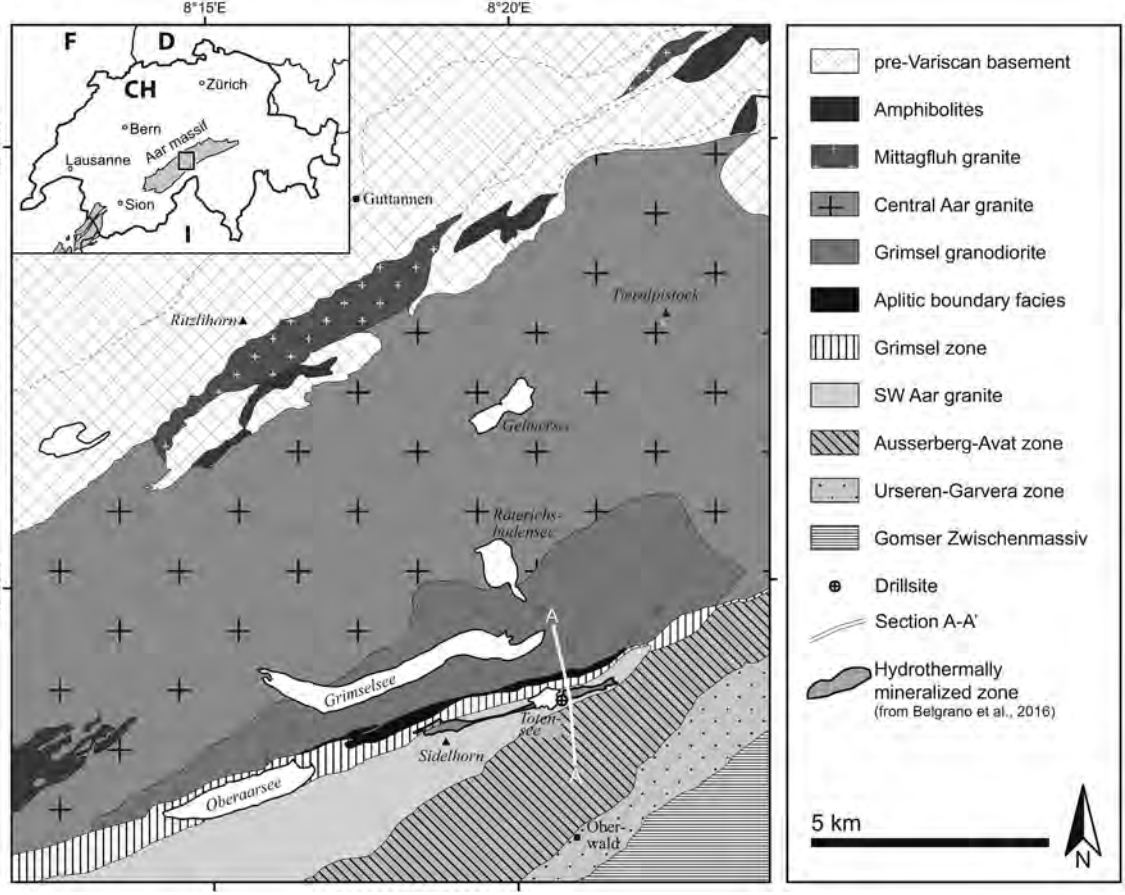
8°15'E
8°20'E
46°40'N
46°35'N
F
D
CH
I
Zürich
Bern
Lausanne
Aar massif
Sion
Guttannen
Ritzlihorn
Tierälpistock
Gelbhorn
Räterichs-
bodensee
Grimselsee
Toten-
see
Sidelhorn
Oberaarsee
Ober-
wald
A
A'
pre-Variscan basement
Amphibolites
Mittagfluh granite
Central Aar granite
Grimsel granodiorite
Aplitic boundary facies
Grimsel zone
SW Aar granite
Ausserberg-Avat zone
Urseren-Garvera zone
Gomser Zwischenmassiv
Drillsite
Section A-A'
Hydrothermally
mineralized zone
(from Belgrano et al., 2016)
5 km
N

Figure 1

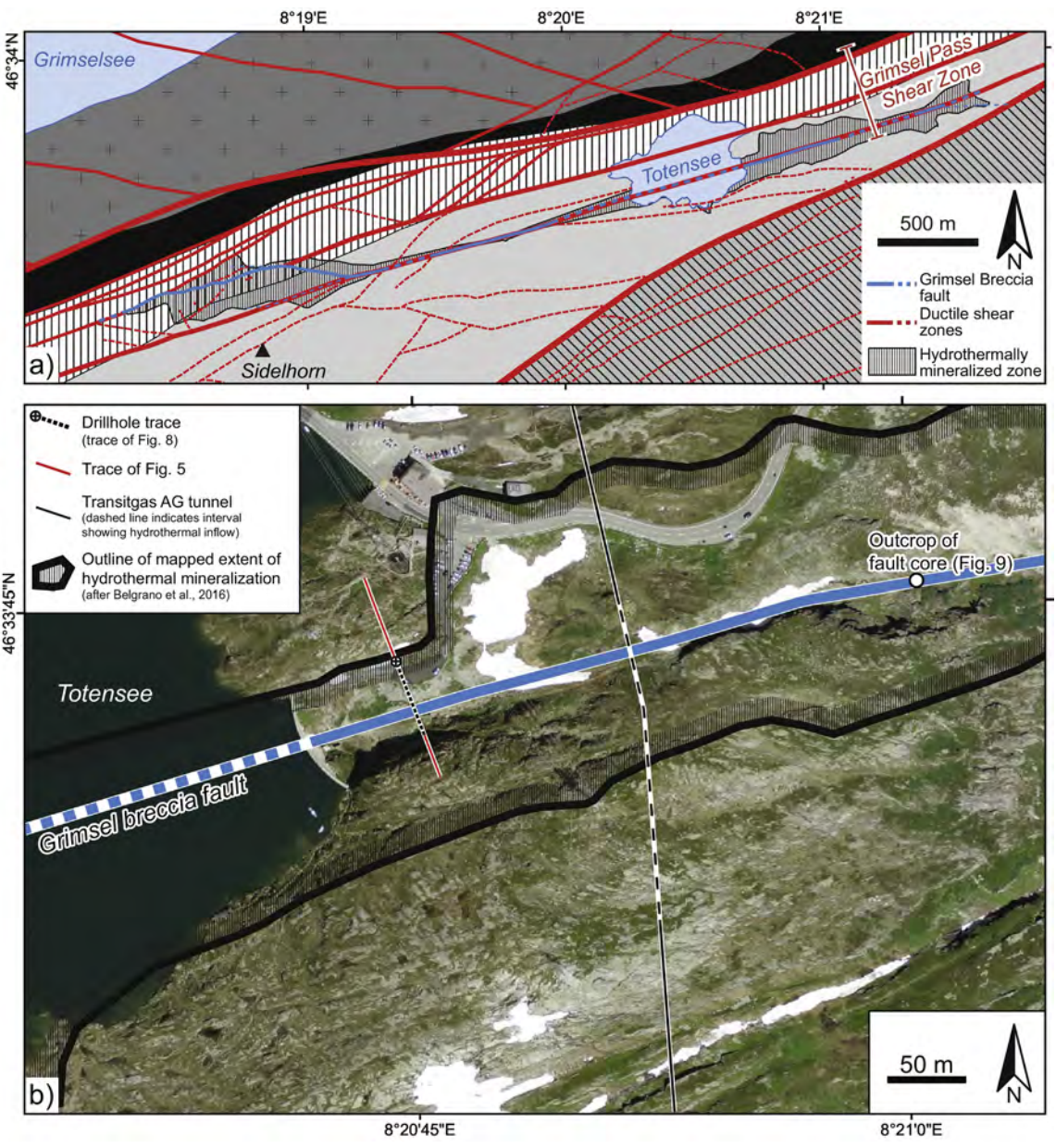
8°19'E
8°20'E
8°21'E
46°34'N
Grimselsee
Grimsel Pass
Shear Zone
Totensee
500 m
N
Grimsel Breccia fault
Ductile shear zones
Hydrothermally mineralized zone
a)
Sidelhorn
Drillhole trace
(trace of Fig. 8)
Trace of Fig. 5
Transitgas AG tunnel
(dashed line indicates interval showing hydrothermal inflow)
Outline of mapped extent of hydrothermal mineralization
(after Belgrano et al., 2016)
Outcrop of fault core (Fig. 9)
46°33'45"N
Totensee
Grimsel breccia fault
50 m
N
b)
8°20'45"E
8°21'0"E

Figure 2

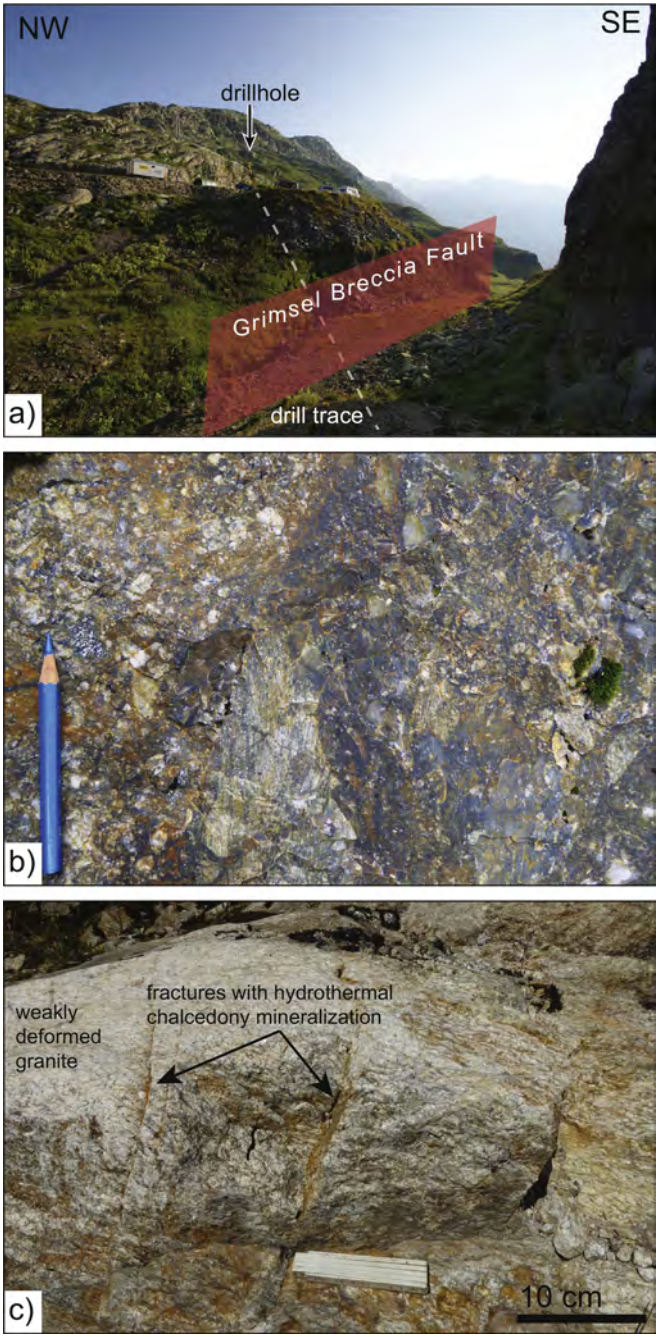
NW
SE
drillhole
Grimsel Breccia Fault
drill trace
a)
b)
weakly deformed granite
fractures with hydrothermal chalcedony mineralization
10 cm
c)

Figure 3

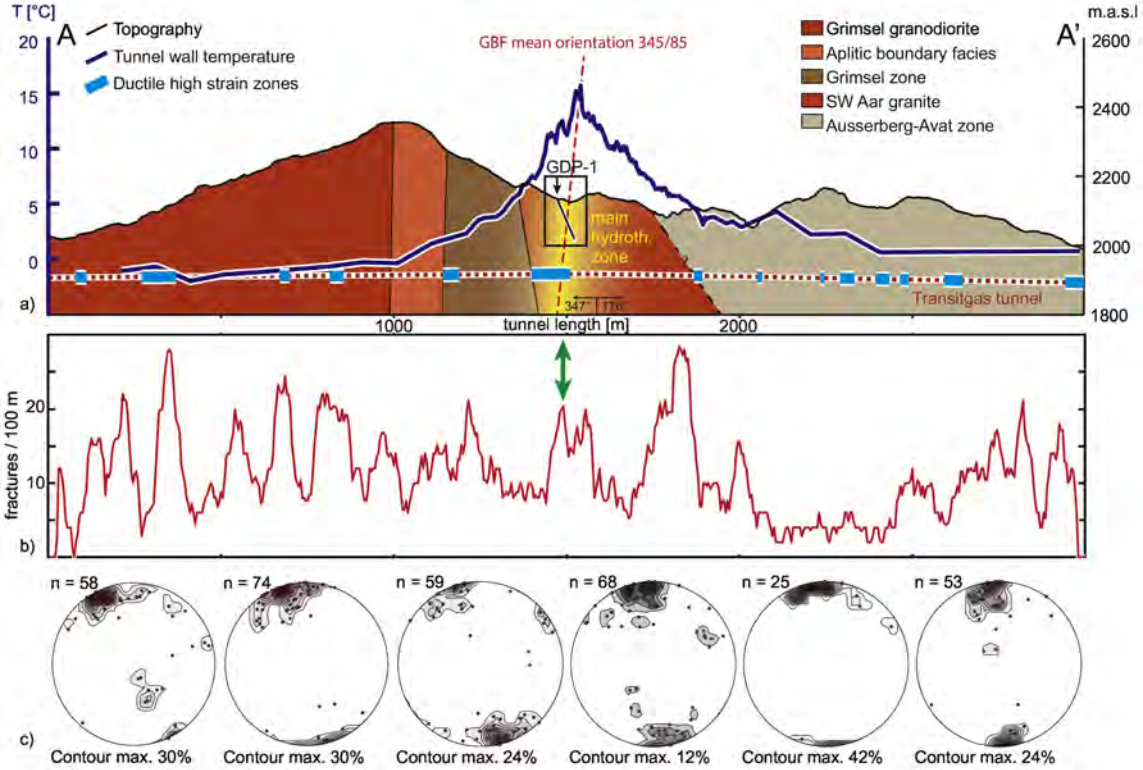
T [°C]
A
A'
m.a.s.l
Topography
Tunnel wall temperature
Ductile high strain zones
GBF mean orientation 345/85
Grimsel granodiorite
Aplitic boundary facies
Grimsel zone
SW Aar granite
Ausserberg-Avat zone
GDP-1
main hydroth. zone
347°
17°
Transitgas tunnel
a)
tunnel length [m]
fractures / 100 m
b)
n = 58
n = 74
n = 59
n = 68
n = 25
n = 53
c)
Contour max. 30%
Contour max. 30%
Contour max. 24%
Contour max. 12%
Contour max. 42%
Contour max. 24%

Figure 4

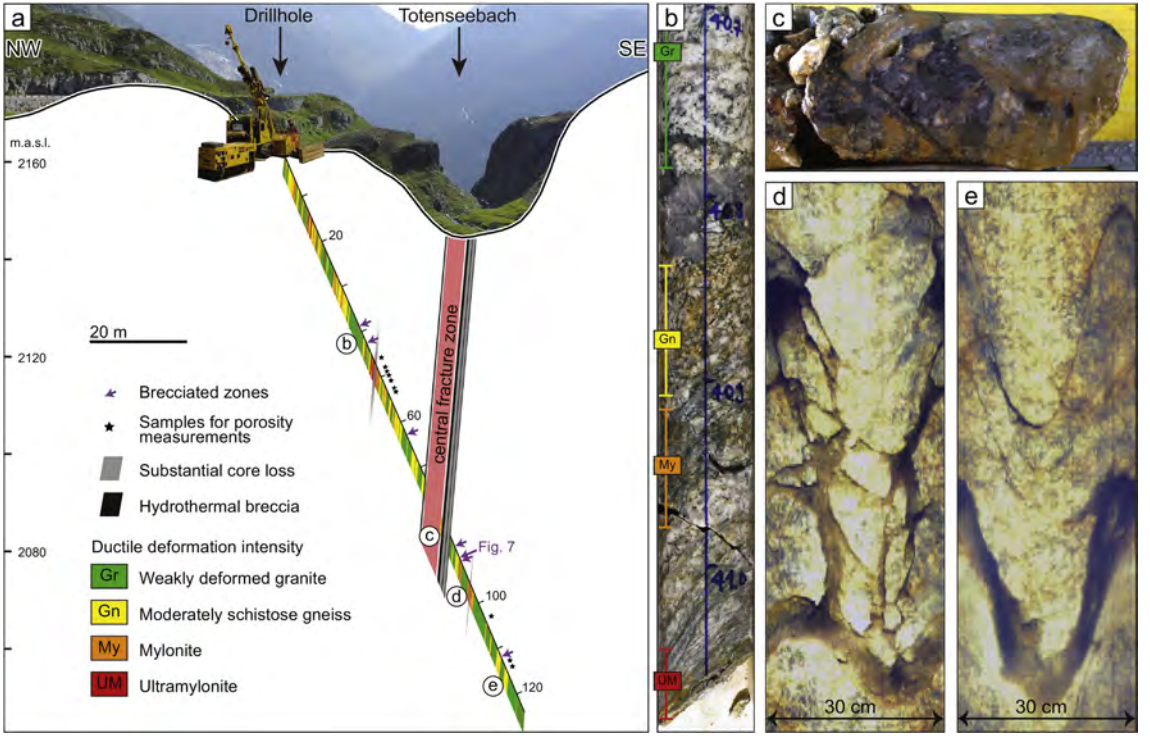
a
Drillhole
Totenseebach
NW
SE
m.a.s.l.
2160
2120
2080
20
60
100
120
20 m
central fracture zone
b
c
d
e
Fig. 7
Brecciated zones
Samples for porosity measurements
Substantial core loss
Hydrothermal breccia
Ductile deformation intensity
Gr Weakly deformed granite
Gn Moderately schistose gneiss
My Mylonite
UM Ultramylonite
b
Gr
Gn
My
UM
c
d
30 cm
e
30 cm

Figure 5

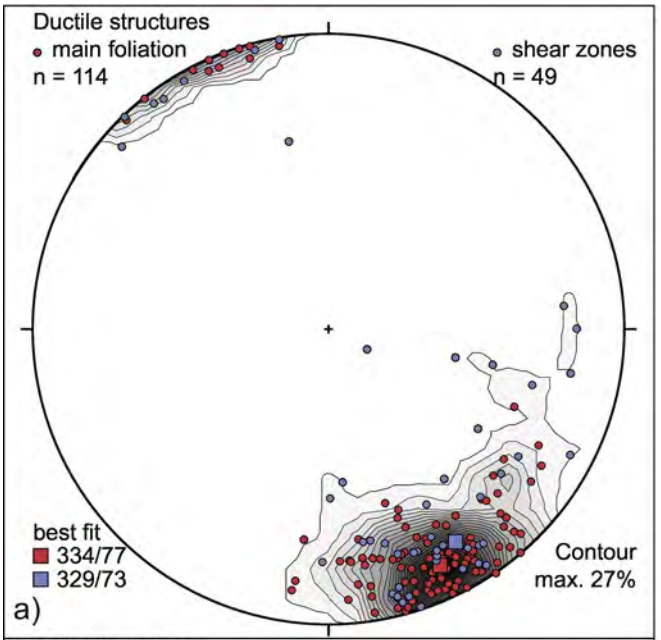
Ductile structures
main foliation
n = 114
shear zones
n = 49
best fit
334/77
329/73
Contour
max. 27%
a)

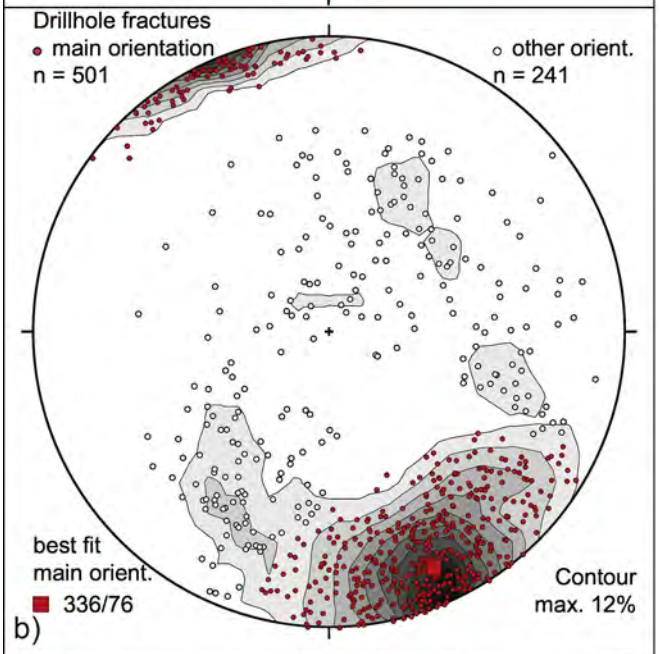
Drillhole fractures
main orientation
n = 501
other orient.
n = 241
best fit
main orient.
336/76
Contour
max. 12%
b)


E
W
~170/85
~140/85
10 cm
c)

Figure 6

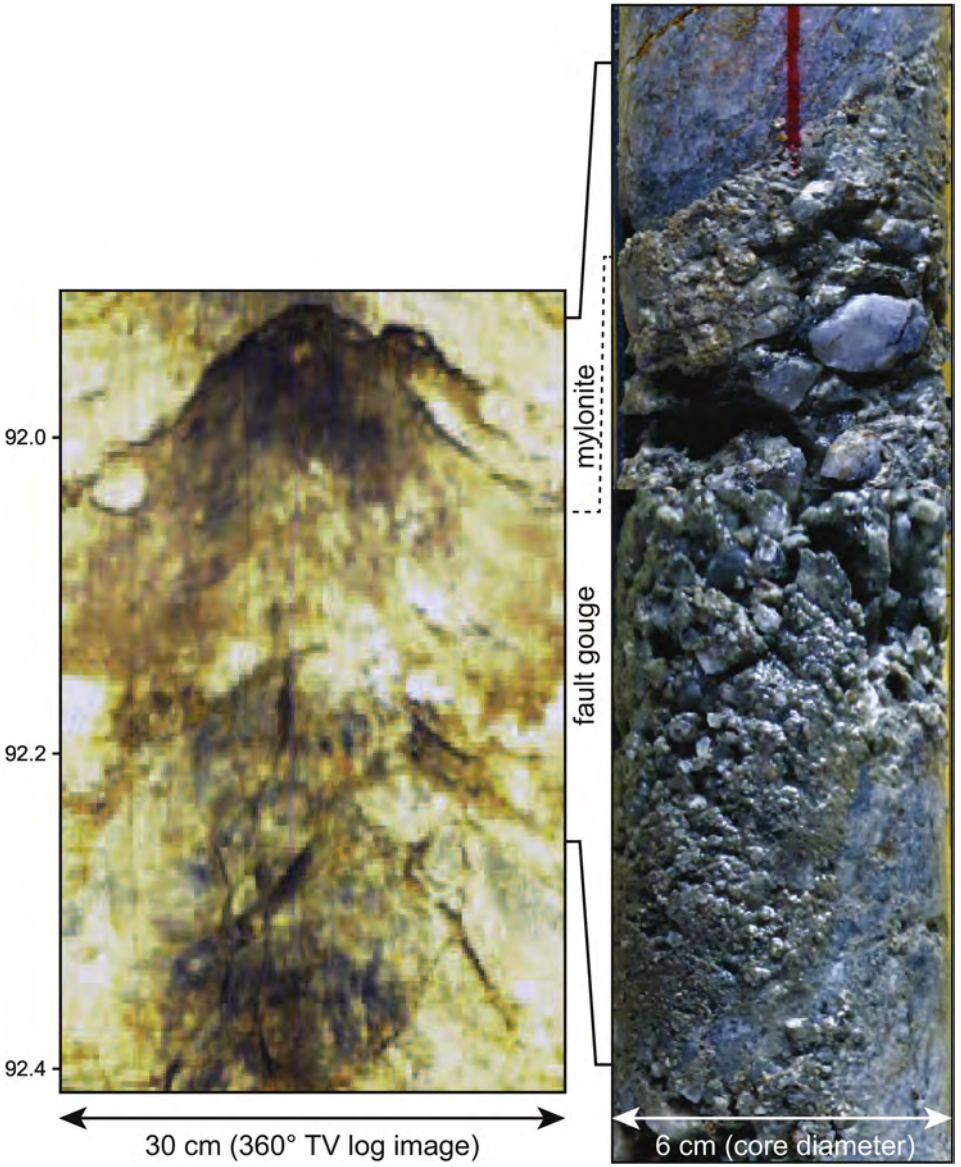
92.0
92.2
92.4
mylonite
fault gouge
30 cm (360° TV log image)
6 cm (core diameter)

Figure 7

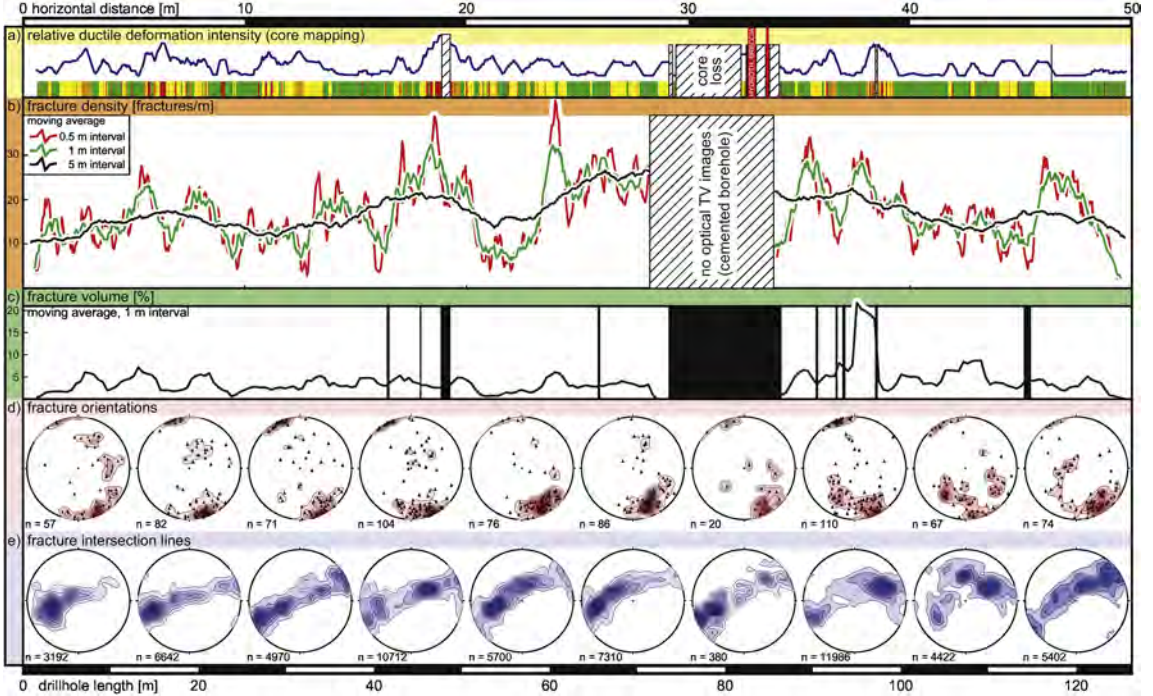
0 horizontal distance [m]
10
20
30
40
50
a) relative ductile deformation intensity (core mapping)
core loss
b) fracture density [fractures/m]
moving average
0.5 m interval
1 m interval
5 m interval
no optical TV images (cemented borehole)
c) fracture volume [%]
moving average, 1 m interval
d) fracture orientations
n = 57
n = 82
n = 71
n = 104
n = 76
n = 86
n = 20
n = 110
n = 67
n = 74
e) fracture intersection lines
n = 3192
n = 6642
n = 4970
n = 10712
n = 5700
n = 7310
n = 380
n = 11986
n = 4422
n = 5402
0 drillhole length [m]
20
40
60
80
100
120

Figure 8

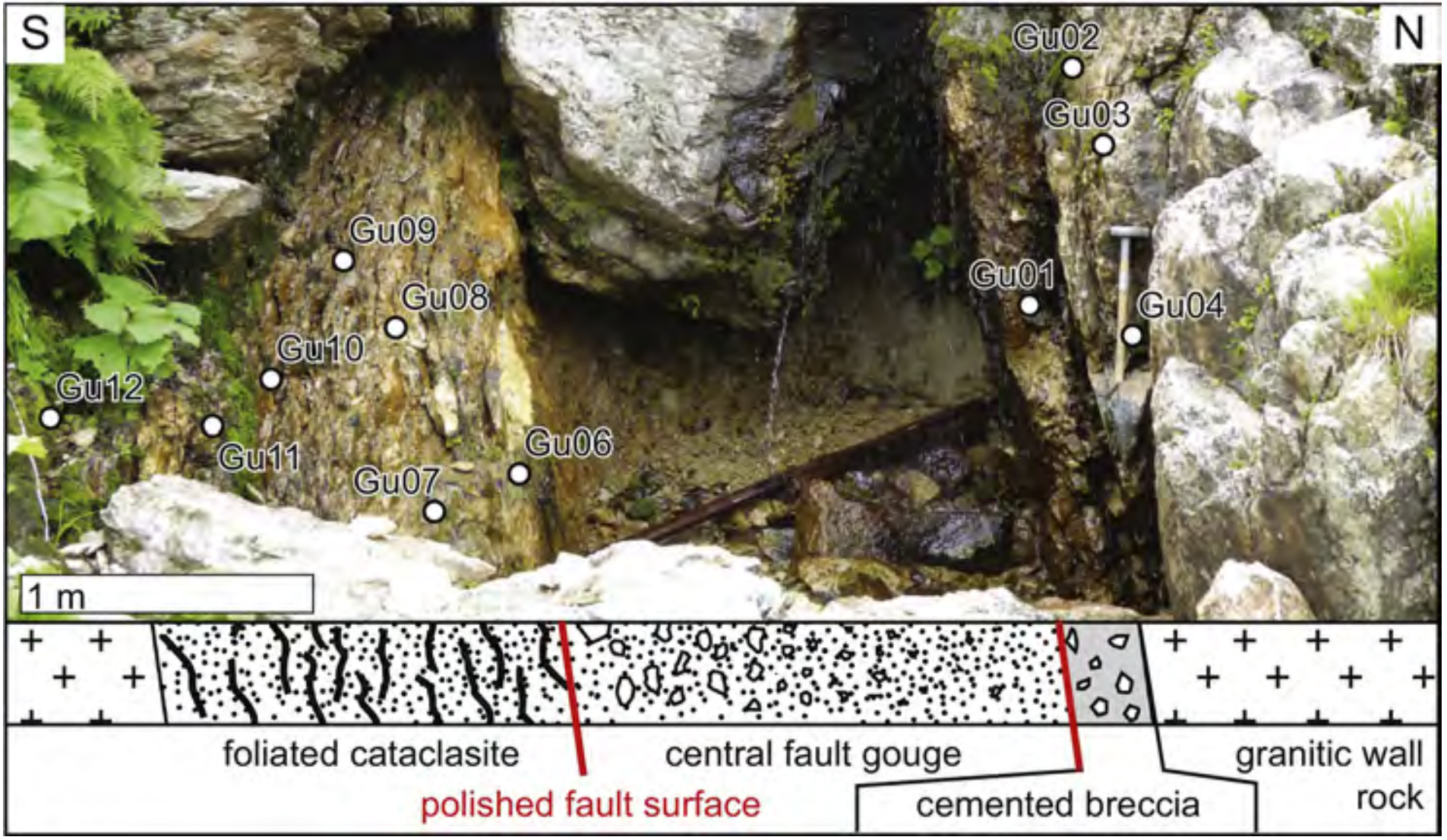
S
N
Gu02
Gu03
Gu09
Gu08
Gu01
Gu04
Gu10
Gu12
Gu11
Gu06
Gu07
1 m
foliated cataclasite
central fault gouge
granitic wall rock
polished fault surface
cemented breccia

Figure 9

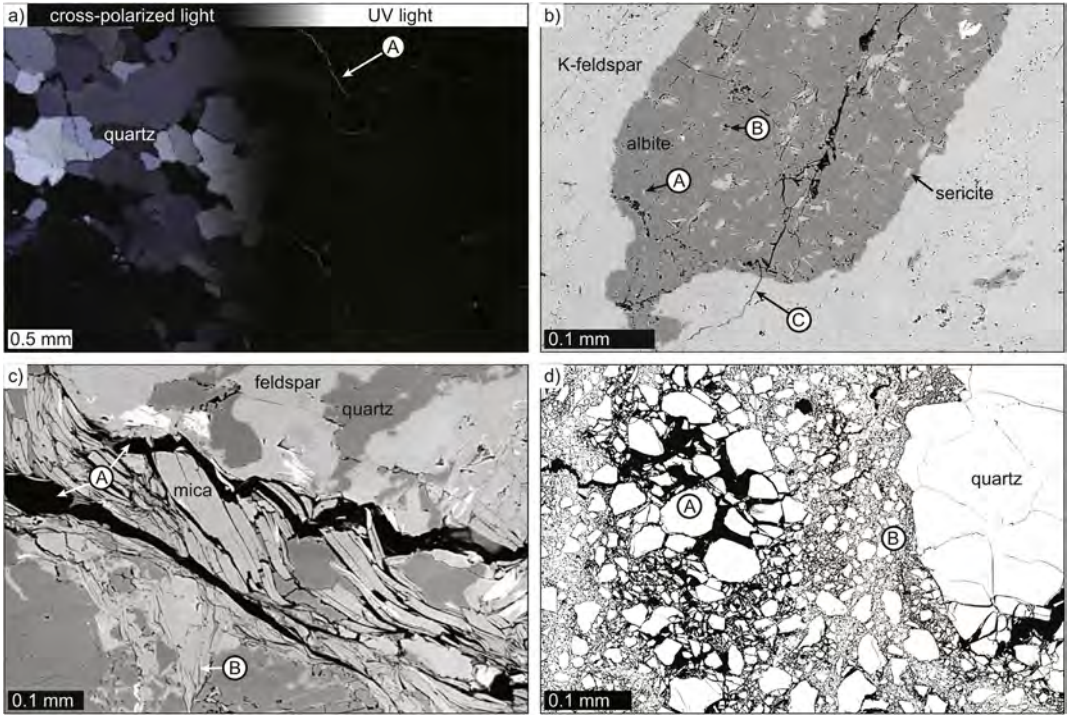
a)
cross-polarized light
UV light
A
quartz
0.5 mm
b)
K-feldspar
B
albite
A
sericite
C
0.1 mm
c)
feldspar
quartz
A
mica
B
0.1 mm
d)
quartz
A
B
0.1 mm

Figure 10

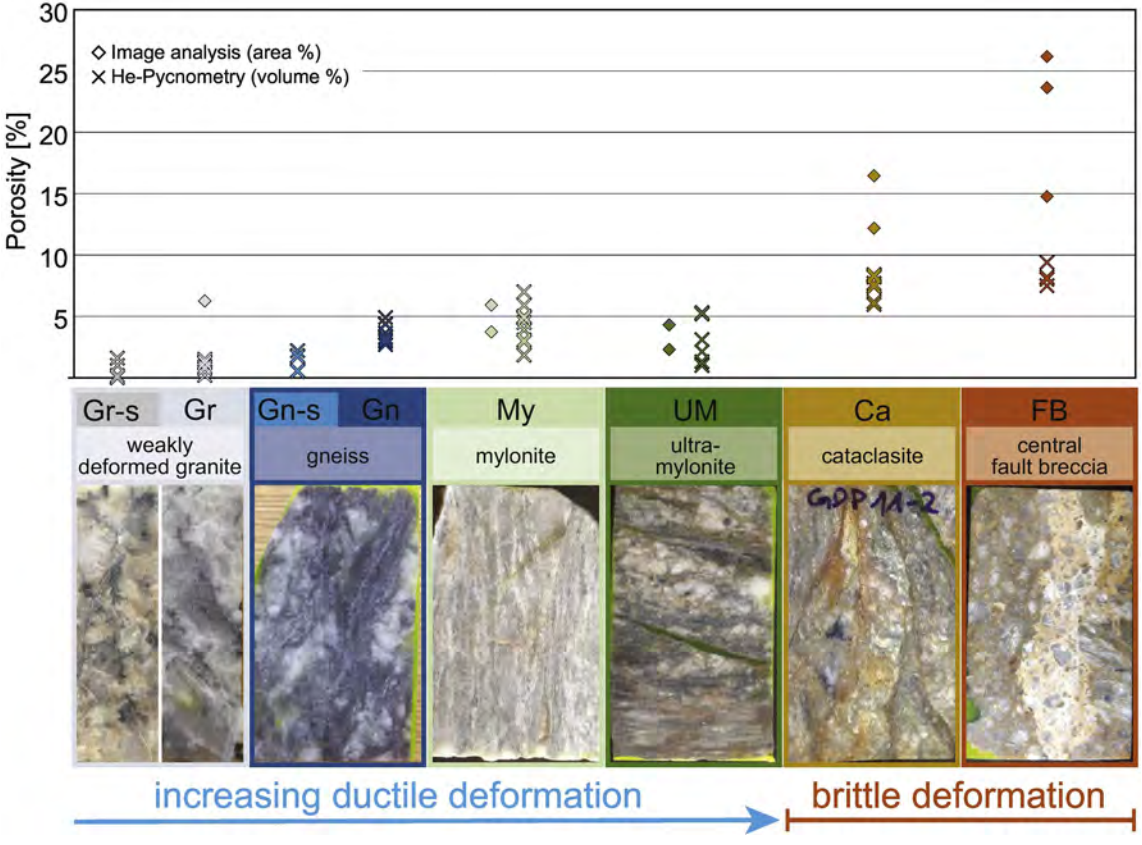
Porosity [%]
30
25
20
15
10
5
◇ Image analysis (area %)
× He-Pycnometry (volume %)
Gr-s
Gr
weakly deformed granite
Gn-s
Gn
gneiss
My
mylonite
UM
ultra-mylonite
Ca
cataclasite
GDP11-2
FB
central fault breccia
increasing ductile deformation
brittle deformation

Figure 11

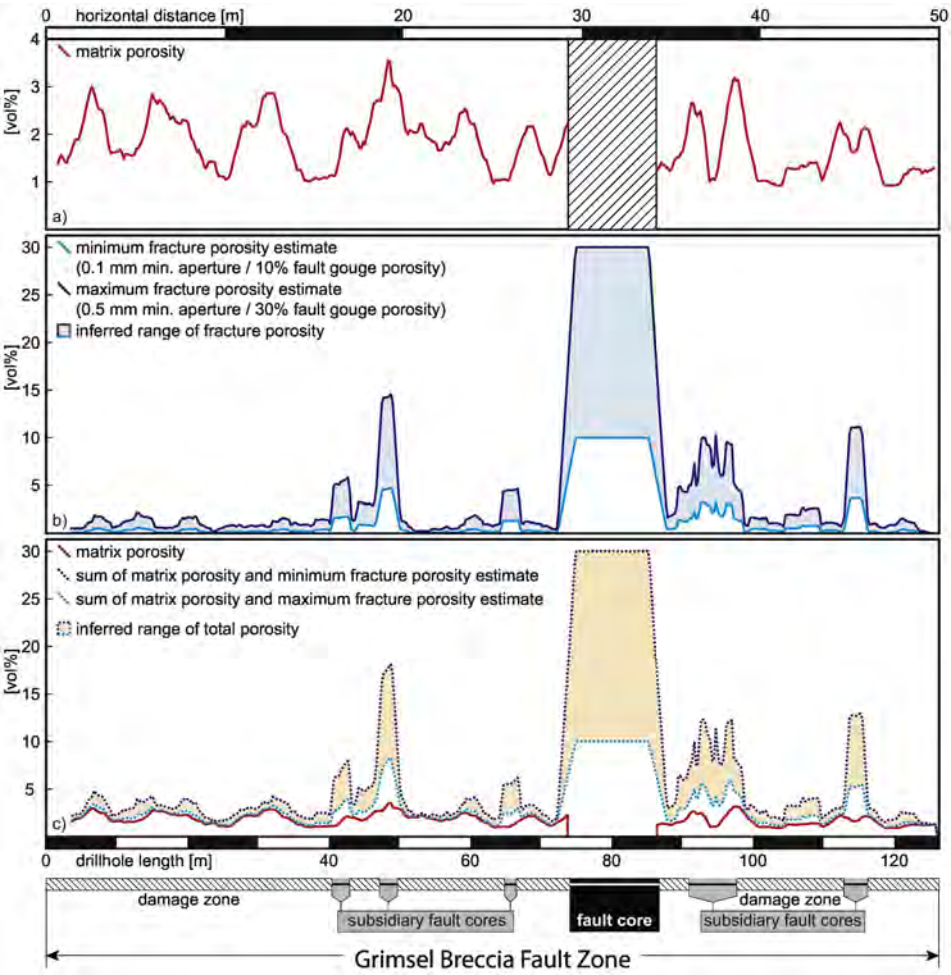
0
horizontal distance [m]
20
30
40
50
matrix porosity
[vol%]
a)
minimum fracture porosity estimate
(0.1 mm min. aperture / 10% fault gouge porosity)
maximum fracture porosity estimate
(0.5 mm min. aperture / 30% fault gouge porosity)
inferred range of fracture porosity
b)
matrix porosity
sum of matrix porosity and minimum fracture porosity estimate
sum of matrix porosity and maximum fracture porosity estimate
inferred range of total porosity
c)
drillhole length [m]
damage zone
subsidiary fault cores
fault core
damage zone
subsidiary fault cores
Grimsel Breccia Fault Zone

Figure 12

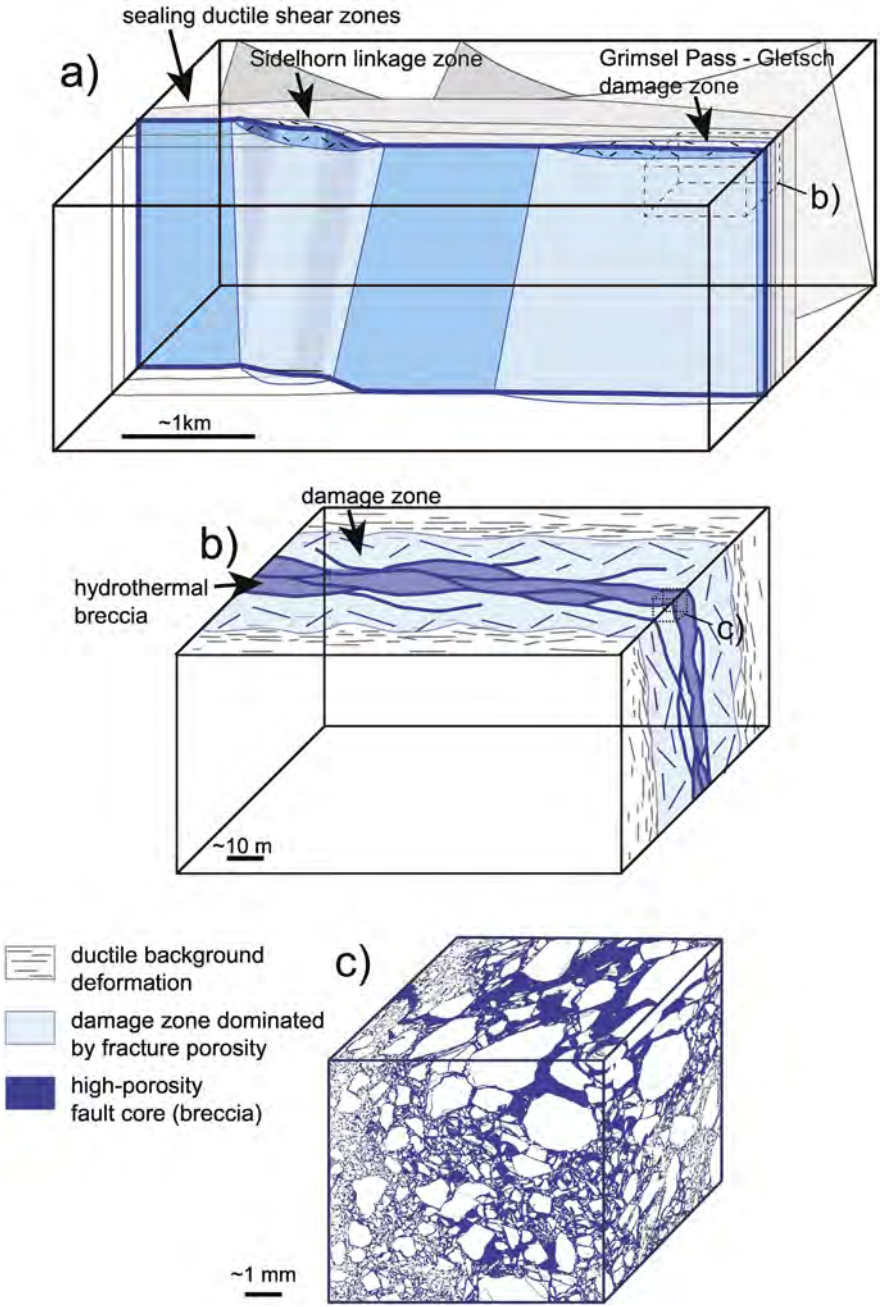
sealing ductile shear zones
a)
Sidelhorn linkage zone
Grimsel Pass - Gletsch
damage zone
b)
~1km
damage zone
b)
hydrothermal
breccia
c)
~10 m
ductile background
deformation
damage zone dominated
by fracture porosity
high-porosity
fault core (breccia)
c)
~1 mm

Figure 13

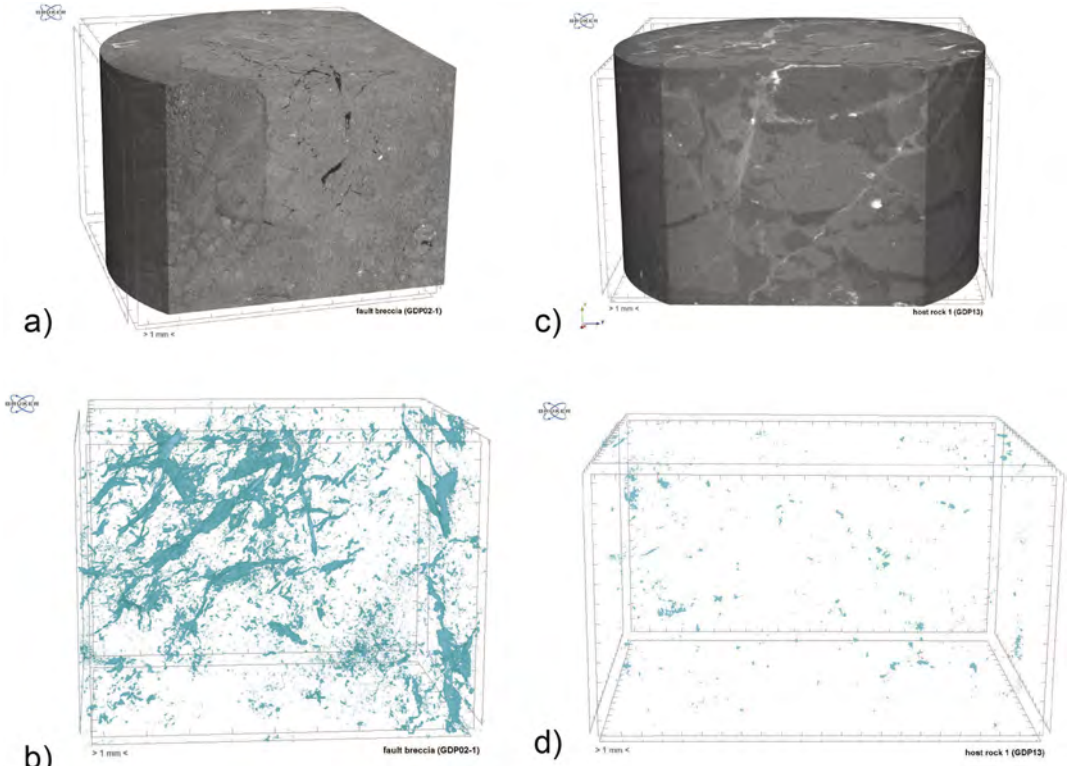
a)
fault breccia (GDP02-1)
> 1 mm <
c)
host rock 1 (GDP13)
> 1 mm <
b)
fault breccia (GDP02-1)
> 1 mm <
d)
host rock 1 (GDP13)
> 1 mm <

Figure 14

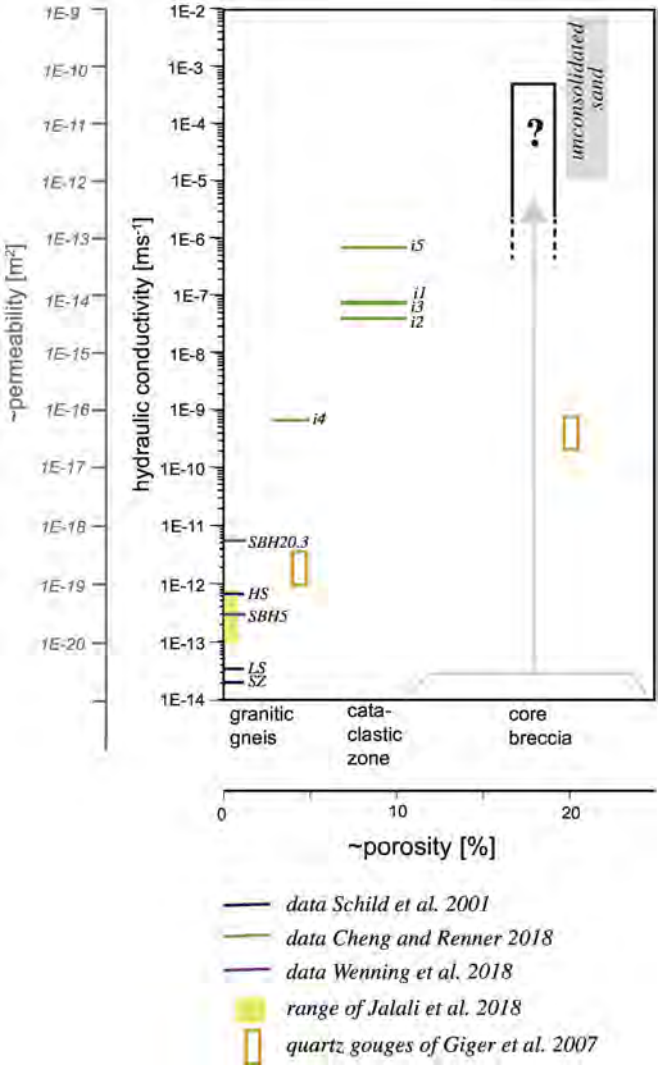
~permeability [m²]
1E-9
1E-10
1E-11
1E-12
1E-13
1E-14
1E-15
1E-16
1E-17
1E-18
1E-19
1E-20
hydraulic conductivity [ms⁻¹]
1E-2
1E-3
1E-4
1E-5
1E-6
1E-7
1E-8
1E-9
1E-10
1E-11
1E-12
1E-13
1E-14
unconsolidated sand
?
i5
i1
i3
i2
i4
SBH20.3
HS
SBH5
LS
SZ
granitic gneis
cata-clastic zone
core breccia
0
10
20
~porosity [%]
data Schild et al. 2001
data Cheng and Renner 2018
data Wenning et al. 2018
range of Jalali et al. 2018
quartz gouges of Giger et al. 2007

Figure 15